Microwave Experiments and Noise in Mesoscopic Devices

Jayanta Sarkar

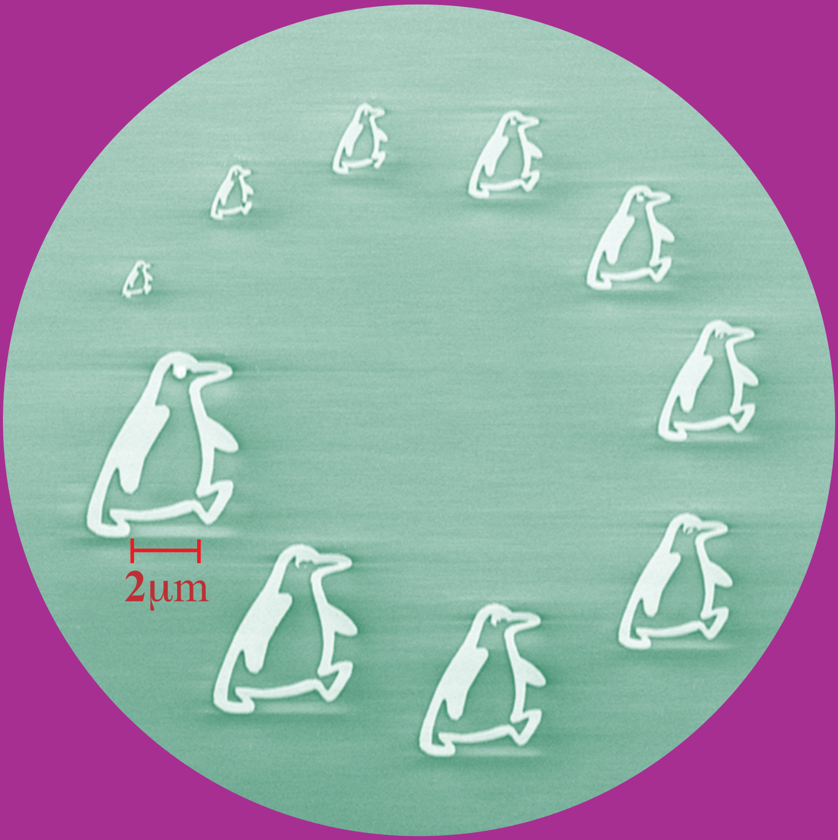

Aalto University

DOCTORAL
DISSERTATIONS

Aalto University publication series
DOCTORAL DISSERTATIONS 69/2015

Microwave Experiments and Noise in Mesoscopic Devices

Jayanta Sarkar

A doctoral dissertation completed for the degree of Doctor of Science (Technology) to be defended, with the permission of the Aalto University School of Science, at a public examination held at the lecture hall AS1 of TUAS on 11th June 2015 at 13:00.

Aalto University
School of Science
Low Temperature Laboratory, Department of Applied Physics
Nano

Supervising professor
Prof. Pertti Hakonen

Thesis advisor
Prof. Pertti Hakonen

Preliminary examiners
Prof. Em. Yuri Galperin, University of Oslo, Norway
Assoc. Prof. Leonid Kuzmin, Chalmers University of Technology, Sweden

Opponent
Dr. Alexander Zorin, Physikalisch-Technische Bundesanstalt (PTB), Germany

Aalto University publication series
DOCTORAL DISSERTATIONS 69/2015

ISBN 978-952-60-6207-5 (printed)
ISBN 978-952-60-6208-2 (pdf)
ISSN-L 1799-4934
ISSN 1799-4934 (printed)
ISSN 1799-4942 (pdf)
http://urn.fi/URN:ISBN:978-952-60-6208-2

Unigrafia Oy
Helsinki 2015

Finland

NORDIC ECOLABEL
441 697
Printed matter

Aalto University

Abstract

Aalto University, P.O. Box 11000, FI-00076 Aalto www.aalto.fi

Author
Jayanta Sarkar

Name of the doctoral dissertation
Microwave Experiments and Noise in Mesoscopic Devices

Publisher School of Science

Unit Low Temperature Laboratory, Department of Applied Physics

Series Aalto University publication series DOCTORAL DISSERTATIONS 69/2015

Field of research Experimental Mesoscopic Physics

Manuscript submitted 7 October 2014 **Date of the defence** 11 June 2015

Permission to publish granted (date) 5 February 2015 **Language** English

☐ **Monograph** ☒ **Article dissertation (summary + original articles)**

Abstract

This thesis is a compilation of several works in the area of condensed matter physics, and with devices based on superconducting Josephson junctions (JJ) as the common denominator for the presented projects apart from the work on diffusive systems. Microwave measurements were conducted on a Superconducting Cooper pair transistor to explore its current-phase relationship. Measurements on a JJ-based qubit coupled to a LC resonator revealed the vibronic transitions obeying the Franck-Condon principle. The main body of the thesis is the work done on the Bloch Oscillating Transistor (BOT), an ultra low noise quantum amplifier. In the present work, we investigated the dynamics of the BOT near the bifurcation threshold as well as implemented differential BOTs to check its capability to reject common mode signals.

To account for our studies of quantum features in mesoscopic systems other than JJs, we performed an experiment similar to the Hanbury-Brown and Twiss interferometry in optics. For this mesoscopic interference experiment we selected a multiterminal diffusive system. We developed a low temperature noise measurement scheme to study current-current correlations in the GHz frequency range. In our experiments we found a small positive HBT exchange correction factor in the non-interacting limit at low bias voltage in the presence of quantum interference. We found negative exchange correction factor in the hot electron case for similar structures, which agrees well with the theory. Altogether, our experiments demonstrated the theoretically predicted HBT exchange effects in non-interacting and interacting regime of electron transport in a diffusive mesoscopic system.

Keywords Low temperature, Bloch Oscillating Transistor, Superconducting Cooper Pair Transistor, Artificial atom, Diffusive system, Shot noise, Current-current correlation

ISBN (printed) 978-952-60-6207-5 **ISBN (pdf)** 978-952-60-6208-2

ISSN-L 1799-4934 **ISSN (printed)** 1799-4934 **ISSN (pdf)** 1799-4942

Location of publisher Helsinki **Location of printing** Helsinki **Year** 2015

Pages 145 **urn** http://urn.fi/URN:ISBN:978-952-60-6208-2

Preface

This thesis was carried out in the Nano Group of the O. V. Lounasmaa Laboratory in the Aalto University School of Science, formerly known as the Helsinki University of Technology. I am sincerely grateful to Prof. Pertti Hakonen for giving me the opportunity of working with several different kind of research projects during my Ph.D. This work would not have been possible without his able guidance in each step of my graduate research work. His depth of knowledge and tireless working style have always acted as inspiration for me. I count myself fortunate to have him as my Ph.D-supervisor. I must thank Prof. Aveek Bid from Indian Institute of Science for introducing me to the Low Temperature Laboratory, where the experiments of my thesis were performed.

Now at the end of my Ph.D journey, when I look back, I feel myself fortunate to be present in the time when two big changes occurred: shifting the lab from Otakaari to Puumiehenkuja, and the change in the name of the university, from Helsinki University of Technology to Aalto University. Being involved in the shifting process gave me an invaluable opportunity to learn plenty of details in assembling various experimental set ups. I encountered many people who have influenced me directly or indirectly, during my stay in the lab. To mention all the names and their influences on my work would take several pages. Nevertheless, I would like to mention some of the individuals whom I encountered.

I would like to express my sincere regards to Prof. Matti Puska and Prof. Sebastian van Dijken for being the acting supervisors at the beginning of my PhD studies. I am thankful to our former director Prof. Mikko Paalanen for his extreme ability to motivate students with cheerful conversations. I am really thankful to our former group members Dr. David Gunarsson, Antti Paila and Dr. Fan Wu, Dr. Lorenz Lechner for helping me in getting used to with the lab environment. I can't forget my wonderful interactions with former post docs of our lab, Dr. Romain Danneau and Dr. Aurelian Fay.

My heartfelt thanks to Antti Puska for not only being a good friend but also a wonderful person to work with. It was a real pleasure to work with him all these years. I will always remember his helpful, generous, kind nature and the attitude to solve different kind of problems. Words fall short in expressing my gratitude to him. My admiration will always be there for Pasi Lähteenmäki for both scientific and non-scientific reasons. Pasi and his car both demand utmost gratitude from my side due to their role in all sort of extra curricular activities which carries almost similar importance as doing science. Many thanks to my group members, Matti Tomi, Dr. Xufeng Song, Mika Oksanen, Dr. Zhenbing Tan, Teemu Nieminen, Jukka-Pekka Kaikkonen for creating a friendly atmosphere. It was always fun to have cheerful discussions with Pasi Häkkinen, Raphael Khan, Daniel Cox and Dr. Manohar Kumar. I also want to thank Dr. Khattiya Chalapat who has always boosted my spirit whenever I felt low.

I wish to express my deepest gratitude to Alexandar Savin who, with his generous smile, was always present whenever needed for solving all sorts of technical difficulties. I am thankful to our secretaries who always kept the lab running smoothly, especially Olga Jakkola, Mari Kaarni, Pirjo Mukkonen and Teija Helme. I was fortunate to work with Juha Hassel in the Bloch Oscillating Transistor project and with Prof Peter Liljeroth on a project on suspended graphene. I would like to thank Prof. Tero Heikkilä and Dr. Pauli Virtanen for all our fruitful scientific discussions. My deepest regards will always be there for Maciej Weisner from Adam Mickiewicz University (Poznan) and Akira Hida from RIKEN (Tokyo). I cherish the moments working with these two wonderful fellows.

Other than my lab people my warm thanks to my friends Kaustuv, Arya, Yadi, Fadi, Tukka, Erkki, Aman, Rakesh, Saurabh, Maryam. I am deeply thankful to Мария for all her inspiring words which undoubtedly helped to carry on this journey. My sincere thanks to Mitali who has always been with me from the beginning of my Ph.D and kept on reminding to stay focussed and work hard. I am extremely grateful to Tony, his wife Ashu, and Lucky for considering me almost as their family member. Their care and affection were always there when needed. Finally, I would like to express my deepest gratitude to my family for being there throughout this endeavour.

Otaniemi, May 4, 2015,

Jayanta Sarkar

Contents

List of Publications

I “Hanbury-Brown and Twiss type exchange effects in four-terminal diffusive conductor.”
Jayanta Sarkar, Antti Puska, Akira Hida, and Pertti J. Hakonen (submitted).

II “Differential Bloch oscillating transistor pair”
Jayanta Sarkar, Antti Puska, Juha Hassel and Pertti J Hakonen, Supercond. Sci. Technol., **26**, 065009 (2013).

III “Dynamics of Bloch oscillating transistor near the bifurcation threshold”
Jayanta Sarkar, Antti Puska, Juha Hassel and P.J.Hakonen, Phys. Rev. B, **87**, 224514 (2013).

IV “Current-Phase Relation and Josephson Inductance of Superconducting Cooper Pair Transistor”
Antti Paila, David Gunnarsson, Jayanta Sarkar, Mika Sillanpää, and Pertti J. Hakonen, Phys. Rev. B, **80**, 144520 (2009).

V “Vibronic spectroscopy of an artificial molecule”
David Gunnarson, Jani Tuorila, Antti Paila, Jayanta Sarkar, Erkki Thuneberg, Yury Makhlin, and Pertti Hakonen, Phys. Rev. Lett., **101**, 256806 (2008).

VI “Interband transitions and interference effects in superconducting qubits”
A. Paila, J. Tuorila, M. Sillanpää, D. Gunnarsson, J. Sarkar, Y. Makhlin, E. Thuneberg, and P. J. Hakonen, Quantum Information Processing, **8**, 245 (2009).

Author's contribution

The main contributions of the author in this thesis lie in the experimental studies on the Bloch Oscillating Transistor and Hanbury-Brown and Twiss interferometry on diffusive systems. I made the samples, performed the measurements, analyzed the data, and wrote the first drafts of publications I, II, III. The author was involved in setting up the dilution refrigerator system *Nanoway* PDR 50 and was the main user of this piece of equipment during 2008-2011. I developed different techniques for sample fabrication, including elaborate four-angle evaporation schemes. In the process of working on shot noise, I shared the responsibility with my 2nd co-author of Publ. I for a 4-K RF-cryostat.

For publications IV, V, VI, my role was active participation in the measurements. As a beginner in this particular field, those projects gave me the background to work with high frequency equipment. I took part in the data analysis with the main author of publication IV. Overall, the involvement with measurements in publications IV, V, VI on Josephson junction based devices gave the author a broad background to carry out the projects of publications I, II, III as the person carrying the main responsibility of all the various research tasks.

1. Introduction

"Meso" is a greek word which means 'middle'. Mesoscopic physics, a branch of condensed matter physics, deals with the systems which belong to intermediate length scales between microscopic and macroscopic. A macroscopic object obeys classical mechanics but when they are scaled down to meso size they start revealing quantum features. Another advantage of studying mesoscopic physics is that, it addresses the several issues due to miniaturization of electronic components, as the physical properties do not remain same in these low dimensional systems.

Initially, the realms of experimental quantum physics were mostly bounded in the area of atomic physics and optics. But due to the advancement in technology, mesocopic physics emerged up as new sub-discipline in the condensed matter physics, which also proved itself as an area to study quantum effects. This area is getting enriched every day both in theoretical and experimental directions.

Perhaps the most profound finding is that in atomic scale the energy levels are discrete, quantized. This quantization can be used for many purposes, for example two levels can serve as two states representing binary information $|1\rangle$ and $|0\rangle$. Scientists have always had a desire to create a custom-made system which is not atomic in size but still exhibits atomic features in the sense of energy levels. A well known and much used device is a Josephson junction (JJ) based qubit with its discrete energy levels.

Many groups are currently working on JJ based qubits with a dream of creating the future quantum computers and, as a bi-product on the way towards that goal, a lot of interesting physics is also explored. This thesis deals with electronic transport focused on mesoscopic systems which I have explored during my doctoral studies. In broad perspective my thesis can be divided into two parts; studies on JJ based devices and current-current correlation investigations on diffusive system.

A major section covered in this thesis is related to Bloch Oscillating transistor (BOT). This device was proven to be a good candidate as a cryogenic current amplifier but the region near the bistability of this amplifier was not thoroughly explored. In this thesis work, this region has been explored in more details yielding new observations (Publ. III). We investigated the common-mode-rejection capability of BOT in differential pair configuration. The low frequency noise spectra of BOT were explored in current gain and transconductance mode.

Another highlight of this thesis is the experiment, commonly known as the Hanbury-Brown and Twiss (HBT) experiment in optics, which was adopted to a diffusive electronic system. The fundamental idea of the HBT type of experiments is measuring *correlations* in *fluctuations*. In a DC measurement one measures the average value of a certain observable, whereas studying fluctuations can give various insight about the fundamental processes occuring in the system. In the context of quantum transport, *noise* [1] is not an unwanted feature for quantum physicists as it gives plenty of insight to various fundamental processes going on in a mesoscopic system. Especially, the shot noise which is dependent on the current flowing through a sample is present in every conductor but it is only measurable as the size of the conductor and the ambient temperature is small enough. By low temperature we generally imply a temperature comparable to or lower than that of liquid helium temperature. Thus during the current-current correlation measurement and shot noise measurements that we have performed at liquid helium temperature the different characteristic length scales were kept in mind.

Current-current correlation reveals many interesting features in different systems. In 1928, Robert Hanbury-Brown and Richard Twiss performed a correlation experiment using photon detectors to determine the radius of a star. Their correlation technique solved the problem of atmospheric disturbances in the measurement scheme of a traditionally used Michelson interferometer. Later on several groups have implemented the idea in solid state physics mostly in 2-dimensional electron gas systems to demonstrate HBT type exchange effects.

We performed the HBT measurement with two sources and two detectors in a four terminal diffusive system. The underlying theory for our experiment was proposed by Blanter and Büttiker [2] and later on Sukhorukov and Loss [3] explained the HBT effect for such a system using semiclassical treatment. In our experiment, we find that the results of HBT experiments for non-interacting and interacting electrons are different. Moreover, we performed a similar experiment with a tunnel junction cross system. Our measurements were performed at liquid helium temperature in the frequency range of $600-900$ MHz which enables us to avoid unwanted $1/f$ noise.

The author also took part in other projects related to Josephson junction based devices (Publ IV, V, VI). Publ. IV describes the current-phase relation in a Superconducting Cooper pair transistor. Publ. V deals with an experimental demonstration of Franck-Condon physics in a qubit coupled to an LC oscillator. The combination of these basic units creates essentially an artificial molecule that was studied at milliKelvin temperatures. Publ. VI deals with an overview of interference effects in superconducting qubits. It describes the physics of the artificial molecule in the phase space picture and Josephson inductance. Moreover, it also describes the Landau-Zener interference in superconducting qubits.

The thesis chapters are organized as follows. In Ch. 2, various theoretical aspects related to current-current correlations are discussed. Ch. 3 describes the sample fabrication related to the major projects (Publs. I, II, III). In Ch. 4, the experimental side of current-current correlation measurement is covered. Chs. 5 and 6 explore the background of superconducting devices followed by the experiments performed at milliKelvin temperatures. All in all, this thesis sums up a wide range of fundamental experiments on mesoscopic devices performed using modern microwave measurement techniques.

2. Current-current correlations in mesoscopic metallic system

2.1 Current noise

From the point of view of electronics, the term “noise" refers to the temporal fluctuations of the current or voltage around the mean value [1]. The Fourier transform of the current-current or voltage-voltage correlation function is a way to characterize these fluctuations. Though many types of noise in an electronic circuitry are undesirable for the device performance e.g., $1/f$ noise, amplifier noise, etc. The intrinsic noise arising due to fundamental transport of charge carriers has always been the focus of interest.

Walter Schottky calculated the noise of a system where the emission of particles takes place independently [4]. In the system where many particles with charge q are transmitted from one lead to another, the probability for N independent tunnel events during time t is given by $P_N(t) = \frac{t^N}{\tau^N N!} q^t/\tau$, where τ is the average time between two tunnel events. For example, in a vacuum diode the average current can be written as $\langle I \rangle = q \langle N \rangle / t$. The noise is proportional to the variance of the number of transmitted particles. Thus noise power in the case of a Poissonian noise source can be written as [5]

$$S = 2q^2(\langle N^2 \rangle - (\langle N \rangle)^2)/t = 2q \langle I \rangle \, . \tag{2.1}$$

The fundamental mathematical tool to explain noise is called *correlation function*. Considering a current passing through a conductor the auto correlation function is defined by

$$C(t') = \frac{1}{T} \int_{-T/2}^{T/2} dt I(t) I(t+t'). \tag{2.2}$$

The spectral density of the noise is given by $S(\omega) = 2 \int_{-\infty}^{\infty} C(t') \exp(-i\omega t') dt'$.

Apparently, q [see Eq. 2.1] might be expected as electronic charge but it is not always the case, but instead it is the effective charge q_{eff} in the process.

For a strongly correlated system, like fractional quantum Hall system, the current is carried by Laughlin quasiparticles which has effective charge $q_{eff} = e\nu$ where $\nu = 2/3, 1/3, 1/5...$ corresponds to the filling factor [6–8]. Hence, shot noise $S_I = 2q_{eff}I$ would be distinct for different filling factors. For normal-superconductor junction, $q_{eff} = 2e$ due to Andreev reflection, which makes the shot noise $S_I = 4eI$.

Another noise which is unavoidable in any measurement is ‘thermal’ noise. It is always present in any resistor above absolute zero temperature. For resistance R, electrical noise due to thermal fluctuations will give rise to voltage fluctuations with voltage spectral density,

$$S_V(0) = 4k_BTR, \tag{2.3}$$

which was first experimentally observed by J.B. Johnson in 1928 [9] along with the theoretical explanation by H. Nyquist [10]. Both of the authors have used the word *‘agitation’* instead of *‘noise’* in their work. Thermal noise and shot noise at low frequency are both white noise[1]. The main difference between these two is that thermal noise is equilibrium noise while latter is out of equilibrium noise; thermal noise depends on the temperature whereas, shot noise varies linearly with the current passing through the conductor. Nevertheless, both of these noises can be considered as ‘white’ in the present work. [2]

In any kind of noise measurement, fluctuations are normally measured using an amplifier with certain gain and bandwidth. In the case of Poissonian noise of Eq. 2.1, the measured quantity is

$$\langle i^2 \rangle_{\Delta f} = S_I(f).G\Delta f = 2eIG\Delta f, \tag{2.4}$$

where I is the average current and $G\Delta f$ is the gain-bandwidth of the measurement [1].

There are several approaches to formulate shot noise for different systems. I only give a short review on the scattering approach.

2.1.1 Scattering approach

In the wave packet (or scattering approach) approach, the current can be considered as superposition of current pulses, [11]

$$I = \sum_n i(t - n\tau)g_n \tag{2.5}$$

---

[1] When the frequencies are less than the inverse relaxation time in the system.

[2] The shot noise to quantum noise cross-over frequency decreases from 6 THz to 0.4 GHz from room temperature to 20 mK. Below this cut-off frequency the shot noise can be considered as white noise.

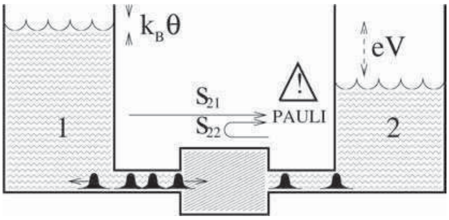

Figure 2.1. Landauer concept of transport; current as a series of pulses (wave packet).[5]

where $i(t - n\tau)$ is the current associated with the n th pulse and where $g_n = +1(-1)$ when the electron is transferred from left(right) to right(left) reservoir and $g_n = 0$ when no transfer takes place.

Landauer was the first to describe the electrical transport as scattering problem [12, 13]. Though it raised doubts at that time but eventually proved to be a strong tool to address many problems in mesoscopic physics. In a macroscopic conductor, the conductance is given by $G = \sigma W/L$, assuming transmission amplitudes are the same for all the transverse modes; here σ is the conductivity and W and L are the width and length of the conductor, respectively. But in smaller dimension, there are corrections to this law. Besides interfacial resistance dependent on L, another factor which affects the conductance is the number of transverse modes in the conductor. According to Landauer, the conductance varies as $G = \frac{e^2}{h}MT$ where M is the number of transverse modes and T is the average probability that an electron injected from one end is transmitted to other end. The net current can be expressed as

$$I = \frac{e^2}{h}MT(\mu_1 - \mu_2), \tag{2.6}$$

where μ_1 and μ_2 denote the chemical potential of the two contacts, respectively.

The milestone laid by Landauer in describing transport in terms of quantum conductance for a two-terminal conductor was later developed by Büttiker for multi-terminal conductors. In this approach, the conductance is determined by a scattering matrix and is commonly known as Landauer-Büttiker formalism [13] which has been successfully used in understanding shot noise for mesoscopic systems [11, 14–16].

Here I describe briefly the Landauer-Büttiker formalism in the case illustrated schematically in Fig. 2.2 to determine various relationships. Suppose the scattering region is connected to ideal reservoirs with given chemical potential μ and temperature T via ideal leads where no scattering takes place. There are transversely quantized modes in the leads. Fig. 2.2 which are connected by the scatterer S in Fig. 2.2. Both channels in each lead contain

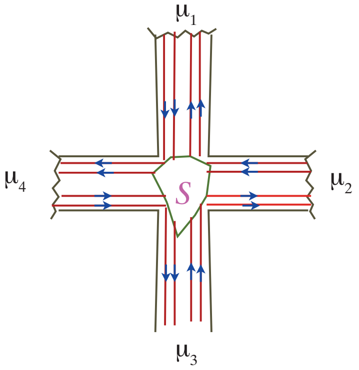

Figure 2.2. Schematic of a four-terminal device with 2 edge modes. Incoming states are scattered by the scattering region.

incoming and outgoing states. After scattering an electron an incoming state is scattered into outgoing states and absorbed by the reservoirs. In the reservoirs, the scattered electrons are finally thermalized. Every occupied mode injects a current from the reservoir into the leads

$$I = \frac{e}{h}\mu. \tag{2.7}$$

Let us denote $T_{ij,mn}$ as the probability that an electron in mode n coming from reservoir j is scattered into mode m of reservoir i. Current-voltage relation can be represented as

$$I_i = \frac{e}{h}\sum_{i\neq j} T_{ij}(\mu_i - \mu_j), \tag{2.8}$$

where $T_{ij} = \sum_{m=1}^{M_i}\sum_{n=1}^{M_j} T_{ij,mn}$. The conductance for a two-terminal conductor can be written as

$$G = \frac{e^2}{h}\sum_{n=1}^{N} T_n, \tag{2.9}$$

where N is the number of occupied channels and T_n is the transmission probability of channel n from one reservoir to the other one.

For a wire with no scattering, the noise is zero. But in the case of $0 < T_n < 1$, the noise expression for a two-terminal conductor at zero temperature takes the form,

$$S_I = 2eV\frac{e^2}{h}\sum_{n=1}^{N} T_n(1 - T_n). \tag{2.10}$$

When $T_n \ll 1$, the above equation yields full shot noise $S_I = 2eI$. In this context, a new ratio is defined, which is called Fano factor in order to describe the suppression or enhancement of shot noise compared to Poissonian noise:

$$F = \frac{S}{S_{poisson}} = \frac{\sum_n T_n(1 - T_n)}{\sum_n T_n}. \tag{2.11}$$

Different characteristics of a mesoscopic system can be accounted for by the particular distributions of transmission eigenvalues T_n. Applications of scattering formalism predicted several interesting features of current spectral density, but also predicted current-current correlations in multi-terminal geometries.

For a two-terminal conductor the current spectral density derived by Büttiker [16, 27] is given by in terms of transmission probability as

$$\begin{aligned} S_I = \frac{e^2}{\pi\hbar}\sum_n \int dE[T_n(E)[f_L(E)(1 \mp f_L(E)) + f_R(E)(1 \mp f_R(E))] \\ \pm T_n(E)[1 - T_n(E)](f_L(E) - f_R(E))^2]. \end{aligned} \tag{2.12}$$

where the first two terms are the equilibrium noise contributions and the third term is the shot noise contribution to the power spectrum. Plus sign in the third term corresponds to fermions whereas minus sign corresponds to bosons. The general expression for a multi-terminal conductor with reservoirs labeled by $\alpha, \beta, \gamma, \delta$ takes the form

$$S_{\alpha\beta} = \frac{e^2}{2\pi\hbar}\sum_{\gamma\neq\delta}\int dE \mathrm{Tr}[s^\dagger_{\alpha\gamma} s_{\alpha\delta} s^\dagger_{\beta\delta} s_{\beta\gamma}]\{f_\gamma(E)[1 - f_\delta(E)] + f_\delta(E)[1 - f_\gamma(E)], \tag{2.13}$$

where s is the scattering matrix [16].

2.1.2 Shot noise of a tunnel junction and a two-terminal diffusive wire

For a tunnel junction, the current spectral density is given by [27]

$$S_I(V,T) = \frac{2eV}{R}\coth\left[\frac{eV}{2k_BT}\right]. \tag{2.14}$$

Eq. 2.14 describes both equilibrium ($V = 0$) noise and out of equilibrium noise. For $eV \ll k_BT$, Eq. 2.14 reduces to Johnson noise $S_I = \frac{4k_BT}{R}$. The general form for a two-terminal system with arbitrary Fano factor (from Ref. [27] with $\sum T_n^2$ written in terms of F) is given by

$$S_I(V,T) = \frac{4k_BT}{R}(1-F) + F\frac{2eV}{R}\coth\left[\frac{eV}{2k_BT}\right], \tag{2.15}$$

which yields Eq. 2.14 with $F = 1$ and

$$S_I(V,T) = \frac{8k_BT}{3R} + \frac{2eV}{3R}\coth\left[\frac{eV}{2k_BT}\right] \tag{2.16}$$

for a two-terminal diffusive conductor with $F = 1/3$. In general, total noise cannot be represented as a simple addition of thermal and shot noise, but rather the noise power is an integral combination of thermal and non-thermal

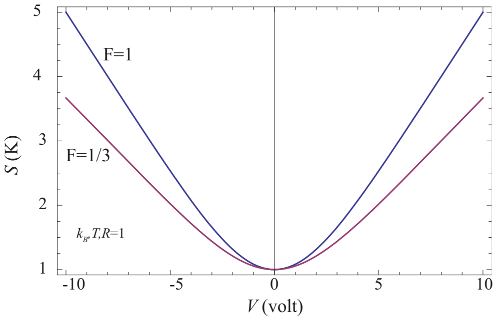

Figure 2.3. Comparison of shot noise between tunnel junction with $F = 1$ and two-terminal diffusive wire with $F = 1/3$. Both has potential to use as shot noise calibration elements.

noise sources. As tunnel junctions and diffusive wires are now well established systems demonstrating $F = 1$ and $1/3$, they can both be used to calibrate a noise measurement set up.

For a two-terminal conductor, auto-correlation and cross-correlation differ only by ‘sign’ but their magnitude remains same. However, for a multi-terminal case there is sign change as well but the magnitude becomes different. Eq. 2.13 is the basis of the correlation measurements in different configurations in a multi-terminal conductor, e.g., diffusive conductor, including Hanbury-Brown and Twiss type of interference phenomena.

2.2 Development of Interferometery: Towards Hanbury Brown Interferometer

Hanbury-Brown and Twiss type of experiments in various branches of science originate from the astrophysics experiments performed in 1950s when R. Hanbury-Brown and R. Q. Twiss built a new type of stellar interferometer to determine the radius of stars [17–19].

When thinking about interferometry, the first notion is the picture of a ‘wave’ yielding constructive or destructive interference patterns. Young’s double slit experiment with light is a textbook topic demonstrating the interference of electromagnetic waves in the wavelength of visible light. This experiment showed that coherent light beams coming from separated slits will interfere and form a pattern on a screen. In 1961, a similar double slit experiment was performed with electrons by Claus von Jönsson [20, 21]. Following von Jönsson’s measurements, several other experiments demonstrated electron’s wave nature to produce interference fringes [22, 23]. Neutrons, atoms and

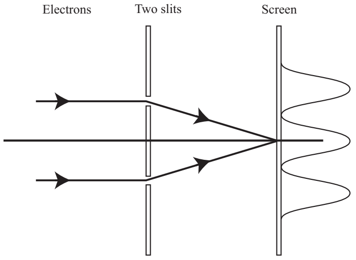

Figure 2.4. Double slit electron interference

molecules have also shown their wave nature in similar experiments later on. These interference phenomena proved convincingly the ‘wave-particle duality’.

Most interference effects of light can be explained with ‘classical’ interpretations. The double slit experiment can be modeled using Huygens-Fresnel principle. When the slit width ‘b’ is greater than the wavelength (λ) of the source light, the intensity pattern of the interference fringes will follow the Fraunhofer diffraction formula

$$I(\theta) = \cos^2\left(\frac{\pi d \sin\theta}{\lambda}\right)\mathrm{sinc}^2\left(\frac{\pi b \sin\theta}{\lambda}\right) \tag{2.17}$$

where d is the separation between the slits.

Interferometric studies have the potential to reveal many interesting phenomena in quantum physics. A quite popular interferometer is the Michelson interferometer. In the Michelson interferometer, a source wave is split into two waves with a beam splitter (similar to slits as in Young’s double slit experiment) and those waves are then interfered after having bounced back from mirrors.

In the Michelson interferometer, we can consider the interference effect between two rays emanating from virtual sources S_1' and S_2' analogous to the two slits of Young’s double slits experiment. In both of the interference experiments the final detection are the ‘fringes’ on a screen. In a similar experiment with electrons, the screen should be electron sensitive in order to create the intensity profile of the ‘fringes’.

The next level of interferometric sophistication is brought by the Hanbury-Brown and Twiss (HBT) interferometer [17–19]. The main difference with this interferometer to the prior ones is the use of two detectors instead of one. In the interferometers prior to the HBT interferometer a photosensitive screen was used to detect the resulting interference pattern. In the HBT interferometer, two photon counters were used and a new technique, ‘correlation’ analysis was implemented between the detected signals [17, 18]. This was a ground breaking technique in interferometric measurements and later on it was picked up in

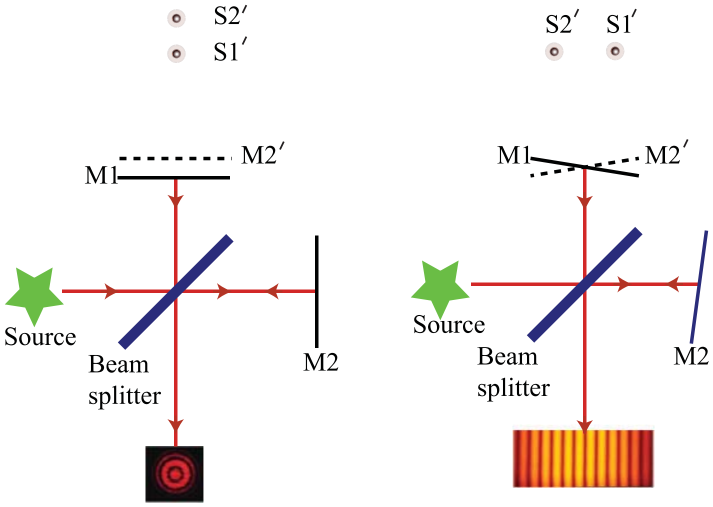

Figure 2.5. Schematic of Michelson interferometry [24].

several branches of physics.

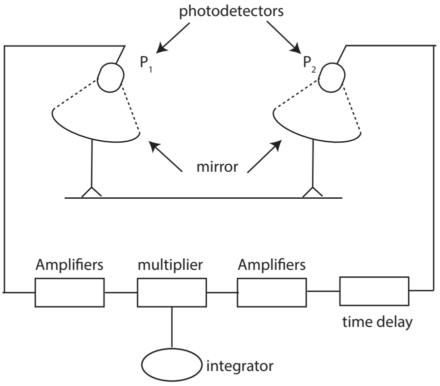

Figure 2.6. Schematic of HBT measurement performed by R. Hanbury-Brown and R. Twiss [17, 18].

After progressing from the experiment using mercury lamp they decided to measure the radius of the star Sirius with this new interferometric technique. They determine the radius of star with great accuracy $0.0068'' \pm 0.0005''$.

The original HBT interferometry is based on intensity-intensity correlations. For a detailed understanding consult Ref. [25]. Here I give a brief account to describe the main features differentiating the Michelson interferometry from HBT interferometry to lay down the great importance of HBT interferometric principle whose importance still prevails even after long time of its first implementation which surpassed all previous interferometric techniques.

In order to focus into the actual working principles of the interferometry by

Robert Hanbury-Brown and Richard Q. Twiss we can consider two photodetectors at points $\mathbf{r_1}$ and $\mathbf{r_2}$ as in Fig. 2.6 the photocurrents can be expressed with the aid of electric field $\mathbf{E_k}$ as

$$I(\mathbf{r_i}, t) \propto |E_\mathbf{k}|^2 + |E_{\mathbf{k}'}|^2 + E_\mathbf{k} E^*_{\mathbf{k}'} e^{i(\mathbf{k}-\mathbf{k}').\mathbf{r_i}} + c.c. (i = 1, 2). \tag{2.18}$$

Multiplying the currents at two detectors yields for the average

$$\begin{aligned} \langle I(\mathbf{r_1}, \mathbf{t}) I(\mathbf{r_2}, \mathbf{t})\rangle \propto & \left[|E_\mathbf{k}|^2 + |E_{\mathbf{k}'}|^2 + E_\mathbf{k} E^*_{\mathbf{k}'} e^{i(\mathbf{k}-\mathbf{k}').\mathbf{r_1}} + c.c.\right] \times \\ & \left[|E_\mathbf{k}|^2 + |E_{\mathbf{k}'}|^2 + E_\mathbf{k} E^*_{\mathbf{k}'} e^{i(\mathbf{k}-\mathbf{k}').\mathbf{r_2}} + c.c.\right] \\ & \propto \left[\langle |E_\mathbf{k}|^2 + |E_{\mathbf{k}'}|^2\rangle\right] \\ & + \langle |E_\mathbf{k}|^2\rangle \langle |E_{\mathbf{k}'}|^2\rangle \left[e^{i(\mathbf{k}-\mathbf{k}').(\mathbf{r_1}-\mathbf{r_2})}\right]. \end{aligned} \tag{2.19}$$

In this result, the low frequency interference term exists but atmospheric sensitive terms $\cos((\mathbf{k}+\mathbf{k}')(\mathbf{r_1}-\mathbf{r_2})/2)$ are absent. This is the main feature of an HBT interferometer.

In a Michelson interferometer, the photocurrent is written as

$$\begin{aligned} & I \propto \langle E^* E\rangle \\ & = \langle |E_\mathbf{k}(e^{i\mathbf{k}.\mathbf{r_1}} + e^{i\mathbf{k}.\mathbf{r_2}}) + E_{\mathbf{k}'}(e^{i\mathbf{k}.\mathbf{r_1}} + e^{i\mathbf{k}.\mathbf{r_2}})|^2\rangle \\ & = \langle 2(|E_\mathbf{k}|^2 + |E_{\mathbf{k}'}|^2) + |E_\mathbf{k}|^2 \left[e^{i.(\mathbf{k}.(\mathbf{r_1}-\mathbf{r_2}))} + c.c.\right] + |E_{\mathbf{k}'}|^2 \left[e^{i.(\mathbf{k}'.(\mathbf{r_1}-\mathbf{r_2}))} + c.c.\right]\rangle \end{aligned} \tag{2.20}$$

For thermal radiation $\langle E_\mathbf{k}\rangle = \langle E_{\mathbf{k}'}\rangle = 0$ and $\langle E^*_\mathbf{k} E_{\mathbf{k}'}\rangle = \langle E^*_\mathbf{k}\rangle \langle E_{\mathbf{k}'}\rangle = 0$. For $\langle |E_\mathbf{k}|^2\rangle = \langle |E_{\mathbf{k}'}|^2\rangle = I_0$, we get

$$I \propto I_0 \left\{1 + \cos\left[(\mathbf{k}+\mathbf{k}').(\mathbf{r_1}-\mathbf{r_2})/2\right] \times \cos\left[(\mathbf{k}-\mathbf{k}').(\mathbf{r_1}-\mathbf{r_2})/2\right]\right\} \tag{2.21}$$

The photocurrent here contains an interference term but environmental fluctuation effects are in $\cos\left[(\mathbf{k}+\mathbf{k}').(\mathbf{r_1}-\mathbf{r_2})/2\right]$ which is the drawback of the Michelson interferometer.

The field operator $\mathbf{E}(\mathbf{r}, t)$ can be written as $\mathbf{E}^{(+)}(\mathbf{r}, t) + \mathbf{E}^{(-)}(\mathbf{r}, t)$ where $\mathbf{E}^{(\pm)}$ are the positive and negative frequency parts. The first order correlation function is then written as

$$G^{(1)}(\mathbf{r_1}, \mathbf{r_2}; \tau) = \langle E^{(-)}(\mathbf{r_1}, t_1) E^{(+)}(\mathbf{r_2}, t_2)\rangle, \tau = t_1 - t_2 \tag{2.22}$$

whereas, the joint probability of photodetection is governed by a second order correlation function $G^{(2)}$ which will be discussed in the next subsection.

2.2.1 Hanbury-Brown and Twiss: Second order coherence

A laser beam and thermal light source can both have the same first order coherence properties but higher order coherence is different. Suppose that there are two independent photons having momentum $\mathbf{k}$ and $\mathbf{k'}$, respectively, then the second order correlation function takes the form

$$G^{(2)}(\mathbf{r_1}, \mathbf{r_2}; t, t) \propto (1 + \cos[(\mathbf{k} - \mathbf{k'})(\mathbf{r_1} - \mathbf{r_2})]. \tag{2.23}$$

For many photon states, e.g., light from stars, the second order correlation takes the form,

$$G^{(2)} \propto \left(2 \langle n \rangle^2 + \langle n \rangle^2 \{1 + \cos[(\mathbf{k} - \mathbf{k'})(\mathbf{r_1} - \mathbf{r_2})]\}\right), \tag{2.24}$$

where $\langle n \rangle = [exp(\hbar\nu/k_B T) - 1]^{-1}$. For fermionic system the correlation function takes the form

$$G^{(2)}(\mathbf{r_1}, \mathbf{r_2}; t, t) = 2 \{1 - \cos[(\mathbf{k} - \mathbf{k'})(\mathbf{r_1} - \mathbf{r_2})]\} \tag{2.25}$$

While the Michelson interferometer at a point $\mathbf{r}$ is observing the average light intensity at time t as $\langle I(\mathbf{r}, t) \rangle = \langle E^{(-)}(\mathbf{r}, t) E^{(+)}(\mathbf{r}, t) \rangle$, an HBT interferometer yields intensity-intensity correlation as $G^{(2)}(\mathbf{r_1}, \mathbf{r_2}; \mathbf{t}, \mathbf{t}) = < E^{(-)}(\mathbf{r_1}, t)$ $E^{(-)}(\mathbf{r_2}, t) E^{(+)}(\mathbf{r_2}, t) E^{(+)}(\mathbf{r_1}, t) >$. Thus, we see that HBT interference works even for two radiative point sources emitting fermions. These would work even for neutrons, beta particles, etc. The only difference would be in different cases the sign of the interference term. A nice demonstration of HBT effect has been extended to systems of atoms too [26].

2.3 Hanbury-Brown Twiss in diffusive system: Diffusive cross and box

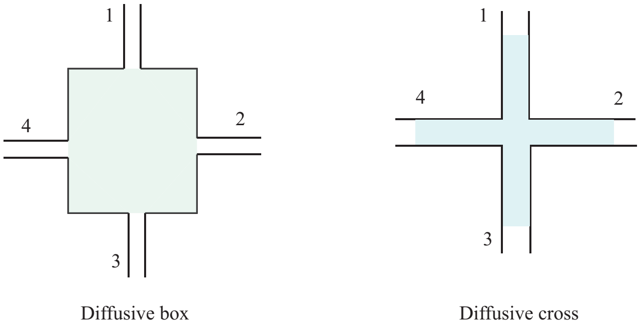

Figure 2.7. Schematic diagram of four-terminal diffusive system. In a diffusive box geometry the shaded area is the main disordered area, whereas in a cross geometry the central area is negligible compared to the area of the arms.

In Ref. [2], Blanter and Büttiker proposed the idea of HBT type of correlations in a multi-terminal diffusive system. They concluded in their theoretical work that the exchange (interference) effect exists in the ensemble-averaged current correlations. They investigated two different kind of structures, namely ‘cross’ and ‘box’ (see Fig. 2.7). The main difference between these two structures is the central area: in the ‘box’ the area is comparably bigger than the arms which implies the shot noise generators are mainly in the central region. In the ‘cross’ the shot noise generators are in the arms of the cross. The contribution of the central area becomes negligible in this case.

Our experimental studies were concentrated on cross shaped structures made of normal metal. The four ends of the cross geometry connected to four ~ 200 nm thick metal leads which acted as reservoirs.

Following the principles from Ref. [2], we have measured the current-current correlation of a cross sample in three different configurations as shown in Fig. 2.8.

- S^A : 1 DC biased. 2, 3, 4 are grounded [3].
- S^B : 3 DC biased. 1, 3, 4 are grounded.
- S^C : 1, 3 DC biased equally. 2, 4 are grounded.

We denote the cross-correlated noise in these configurations A, B, C as S^σ with $\sigma = A, B, C$:

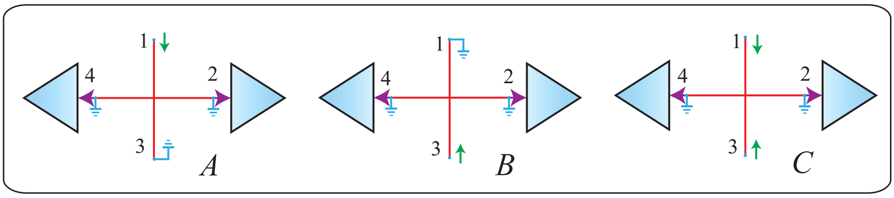

Figure 2.8. Measuring and biasing configurations to demonstrate electronic HBT effect in a four-terminal system.

$$\begin{Bmatrix} S^A \\ S^B \\ S^C \end{Bmatrix} = \frac{e^2}{\pi} e|V| \begin{Bmatrix} \Xi_1 \\ \Xi_2 \\ \Xi_1 + \Xi_2 + \Xi_3 + \Xi_4 \end{Bmatrix}, \tag{2.26}$$

where the terms $\Xi_i (i = 1, 2, 3, 4)$ are fluctuations of the scattering matrices [2, 27]. Due to the interference terms Ξ_3 and Ξ_4, the addition of S^A and S^B does not amount to S^C. In the above mentioned definition S^A, S^B, S^C are defined as positive quantities. Ξ_3 and Ξ_4 are named as exchange terms, whereas the difference of S^C to $(S^A + S^B)$ is named as ‘exchange correction

---

[3] Grounded at DC but not at $f \gg 10$ kHz. The terminals are grounded through bias-tees.

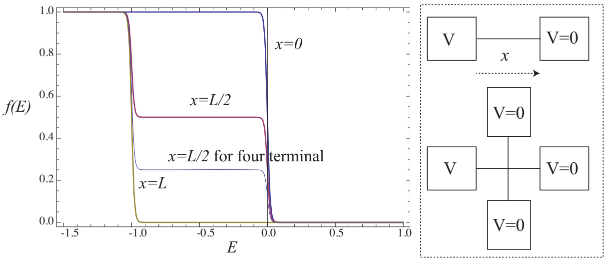

Figure 2.9. Fermi distribution function along a diffusive wire for two-terminal case and four-terminal case (e.g.,A, B configurations discussed in previous section). At the center of the cross $f(E)$ in the four-terminal system is half of the two-terminal case. Although, for C configuration with two biased and two ground terminals, the distribution reduces to the two-terminal case.

factor' ΔS:

$$\Delta S = S^C - S^B - S^A \tag{2.27}$$

Due to $\Xi_3 + \Xi_4$ in S^C, ΔS does not necessarily become zero. In a finite-size 'cross' shaped geometry ΔS can be positive.

2.4 Semiclassical theory for shot noise in a multi-terminal diffusive conductor

Suppression of shot noise in a diffusive conductor has been modeled using different theoretical techniques; scattering matrix approach, Green's function technique, semiclassical Boltzmann-Langevin approach. All of the techniques ended up with the same result that the suppression factor for a two-terminal diffusive system is 1/3. In the semiclassical theory, the quantum phase coherent effect is not included in the analysis. For a multi-terminal conductor, the suppression factor depends on the sample configuration and geometry. Sukhorokuv and Loss [3]have addressed the issue of noise correlations in a multi-terminal diffusive conductor and calculated suppression factors in different geometries.

The spectral density of current fluctuations between terminal m and n of a multi-terminal system is given by $S_{nm} = \frac{1}{2}\int dt\, \langle \delta I_n(t)\delta I_m(0) + \delta I_m(t)\delta I_n(0)\rangle$ at zero frequency, where m and n label the terminals. For $n = m$, this denotes the autocorrelator of current fluctuations S_{nn} which can be expressed as FeI_n using the Fano factor F. For $n \neq m$, S_{nm} denotes the cross-correlated noise between leads n and m; usually negative in fermionic systems but though possibly also positive due to interactions [28].

In the semiclassical theory [3], the spectral density of noise in a diffusive system is governed by $\Pi(\mathbf{r}) = 2\int d\epsilon f_0(\epsilon,\mathbf{r})[1 - f_0(\epsilon,\mathbf{r})]$, where f_0 is the local distribution function. In the noninteracting regime, $f_0 = \sum_n \phi_n f(\epsilon - eV_n)$, where ϕ_ns are characteristic potentials, induced by terminal voltages V_n and $f(\epsilon)$ the Fermi functions of the reservoirs. $\Pi(\mathbf{r})$ then takes the form of $2\int d\epsilon \sum_{k,l} \phi_k\phi_l f(\epsilon - eV_k)[1 - f(\epsilon - eV_l)]$. Spectral density of noise is related to $\Pi(\mathbf{r})$ through $S_{nm} = \int d\mathbf{r}\nabla\phi_n.\hat{\sigma}\nabla\phi_m\Pi$, where σ is the conductivity tensor. When electron-electron interactions smear the coherent double-step distribution function, $f_0(\epsilon,\mathbf{r})$ takes the form of a Fermi distribution $f_0(\epsilon,\mathbf{r}) = (1 + \exp[(\epsilon - eV(\mathbf{r}))/(k_BT_e(\mathbf{r}))])^{-\mathbf{1}}$. Essentially, the distribution function, which governs the “energy" integral $\Pi(\mathbf{r})$, differentiates the non-interacting and interacting regimes with distinct correlated noise powers.

Without interference, the bias dependence of the HBT effect can be accounted for by the semiclassical approach for a diffusive cross in a non-interacting regime where the current fluctuation spectrum takes the form [3],

$$\begin{aligned} S_{nm}(V) &= \tfrac{1}{3}2e\sum_k \alpha_n\alpha_k(J_k + J_n)(\delta_{nm} - \delta_{km}) \\ &\qquad -\tfrac{4}{3}G_{nm}k_BT, \end{aligned} \tag{2.28}$$

where $J_n = \sum_l G_l(V_n - V_l)\coth\left(\frac{e(V_n - V_l)}{2k_BT}\right)$ and $\alpha_m = G_m/\sum_n G_n \equiv G_m/G$.

The exchange correction determined from the semiclassical theory [3, 29] includes the thermal HBT exchange which is explained in Publ. III. Overall, semiclassical theory explains the region where interference does not play a role.

In addition to the exchange effect, the semiclassical theory also addresses some extra features e.g., ‘universality’, and ‘nonlocality’ of noise. In the following subsection, I will tell about ‘universality’ of F, the reduction of F in different bias configurations and the ‘nonlocality’ of shot noise.

2.4.1 Universality of Fano factor

In a multi-terminal diffusive conductor with one lead biased ($V_1 = V$) and the rest grounded ($V_n = 0, n \neq 1$), the shot noise expression takes the form:

$$S_{1n} = -\frac{1}{3}2G_{1n}\left[4k_BT + eV_1\coth\left(\frac{eV_1}{2k_BT}\right)\right]. \tag{2.29}$$

At $T = 0$,

$$S_{1n} = -\frac{1}{3}2e|I_n|, n \neq 1, \tag{2.30}$$

$$S_{11} = \frac{1}{3}2e|I_1|. \tag{2.31}$$

The above expression is valid for arbitrarily shaped conductors. The suppression factor is the same as for a two-terminal diffusive conductor where the suppression factor is 1/3. In short, the shot noise measured with respect to the total current is independent of the sample configuration as long as the biasing port and measuring port are same and rest of the leads are grounded.

2.4.2 Suppression of Fano factor from 1/3

For auto-correlation, we need to calculate S_{nn} while for the correlated part of the noises between two terminals, we need to calculate S_{nm}.

While measuring the cross-correlated, noise the suppression factor is different in different configurations. When the biasing end is terminal 1, the current-current correlations take the form:

$$S_{11} = \frac{1}{3} 2eI \tag{2.32}$$

$$S_{12} = S_{13} = S_{14} = -\frac{1}{9} 2eI \tag{2.33}$$

$$S_{22} = S_{33} = S_{44} = \frac{2}{9} 2eI \tag{2.34}$$

$$S_{23} = S_{24} = S_{34} = -\frac{1}{18} 2eI \tag{2.35}$$

We have performed successful measurements to find the suppression factor from the auto-correlation and cross-correlation measurements, and found complete agreement with the theoretical predictions. To keep the thesis concise, we are not going to present the data and leave it for a future publication.

3. Sample fabrication

3.1 Introduction

Sample fabrication is a major task in experimental mesoscopic physics. As the size shrinks the fabrication becomes more complicated. To just study a thin film, we don't need any lithographic processes. A simple quartz crystal is enough to monitor the thickness of a thin film during evaporation. But to pattern the film to make a more complicated geometry, one needs suitable lithographic tehniques. To get a desired structure bigger than 1μm, photolithography is an appropriate technique. To reach sub-micron features, e-beam lithography or equivalent is needed.

This thesis deals mainly with two different kind of samples: diffusive multi/two-terminal devices and Josephson junction based systems. I first explain the fabrication procedure of the diffusive structures.

3.2 Thin wires with thick reservoirs

To fabricate narrow linewidth structures normally people use thin layer of resist and high accelerating voltage for lithography to avoid back scattered electrons. But that process was not suitable for our purpose as we opted for a device which involves two drastically different thicknesses in a single structure. One way is to fabricate the thin structure on a substrate with pre-patterned alignment markers with thin resist first followed by thick structures with bilayer resist. However, we found that it is best to to fabricate the structure in a single lithographic process.

3.2.1 Fabrication process for two-terminal diffusive wire

First, 10% copolymer and 3% PMMA were spun on oxidized Si substrate. Each polymer coating step was followed by baking at 180C for 30 min. Hard baking allows us to achieve narrow linewidth structures. After e-beam exposure the chips were developed with MIBK:IPA (1:4) mixture followed by drying with nitrogen gas. These chips were subjected to evaporation of thin metal perpendicular to the substrate surface (see Fig. 3.1). We have used 2 nm of Ti layer as a sticking layer. The schematic fabrication process is shown in Fig. 3.1. Thick reservoirs were evaporated with the sample stage tilted $\gtrsim 40^0$ (with respect to source-sample axis). In this step, the evaporated metal does not enter through the narrow window of the fine structure, rather it piles up on the wall of the resist. Thus, two angle evaporation procedure enabled us to fabricate a thin wire with thick pads.

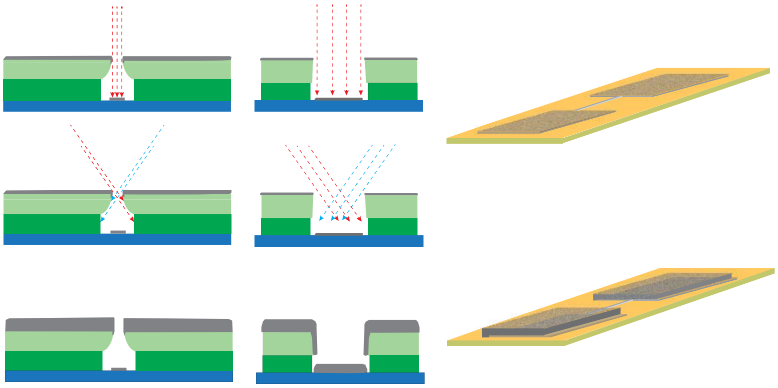

Figure 3.1. Schematic view of evaporation process for two-terminal wire with 200-nm thick reservoirs.

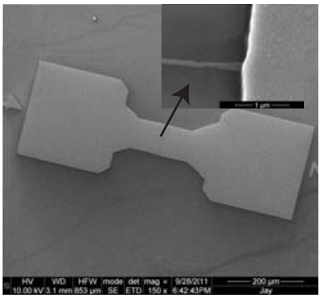

Figure 3.2. SEM image of a two-terminal diffusive wire with thick reservoirs.

3.2.2 Cross-shaped structure

The recipe discussed above for the two-terminal wire fabrication uses resists which react with the same developer, which takes away some freedom in fabrication. Therefore, we used ZEP as the top layer and PMMA 50K as the bottom layer in order to develop each layer selectively. PMMA can be developed with MIBK and ZEP-N50 with n-Amyl acetate. n-Amyl acetate (MIBK) does not react with PMMA (ZEP) which made it possible to control the development of each layer separately. ZEP resist being more sensitive than PMMA, needs less e-beam dose for lithography. With this bilayer resist combination, even 20 kV accelerating voltage resulted in < 100 nm line width with high yield.

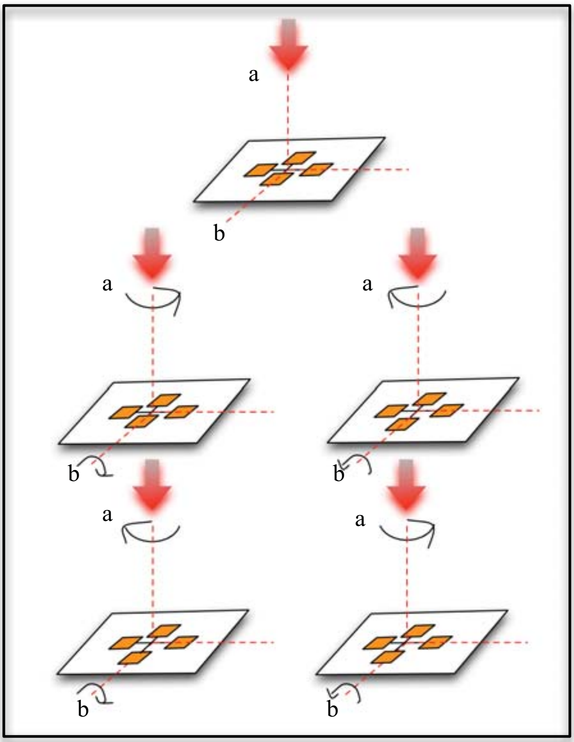

Figure 3.3. Evaporation steps for diffusive cross.

The evaporation steps for cross-shaped fine structure with thicker reservoirs is shown in Fig. 3.3.

- zero angle evaporation of sticking layer (~ 2 nm Ti) followed by metal of the desired thickness (~ 10 nm Cu) for diffusive cross structure
- rotate the stage $+45^0$ and tilt by $+40^0$
- evaporation of metal: ~ 50 nm
- rotate the stage -45^0 and tilt by -40^0

- evaporation of metal: ~ 50 nm
- rotate the stage $+45^0$ and tilt by -40^0
- evaporation of metal: ~ 50 nm
- rotate the stage -45^0 and tilt by $+40^0$
- evaporation of metal: ~ 50 nm
- lift off in warm acetone followed by rinsing in Iso-propanol and drying with nitrogen blower.

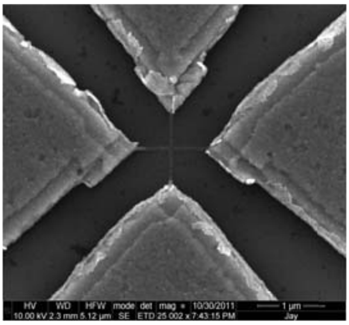

Figure 3.4. SEM image of thin cross structured sample with 200 -nm thick reservoirs.

3.3 Tunnel junction fabrication

Ultra-small-normal metal or superconducting tunnel junctions require e-beam lithographic processing. Large tunnel junctions can be fabricated using photo lithography. We used 3% PMMA as the top layer and 10% MMA/MAA (copolymer) as the bottom layer for our bilayer resist combination. In principle, the evaporation procedure is similar to the fabrication process of ‘wire’ but no zero angle evaporation is involved in this case. Thus, no requirement of very narrow linewidth in the mask (say 100 nm) to fabricate sub-100nm size junctions. The shadow evaporation takes care of the reduction of the size. The design and evaporation technique is illustrated in Fig. 3.5. After the first evaporation of 20 nm of Al at a tilting angle of $+24^0$ the sample is moved to load lock for oxidation in a Ar/O_2 mixture for 90 s. After that the load lock is evacuated well and the sample is put back into main chamber followed by evaporation of 40 nm of Al at an angle of -24^0. The sample is subjected to lift off in warm acetone and rinsed with IPA followed by drying with nitrogen blower.

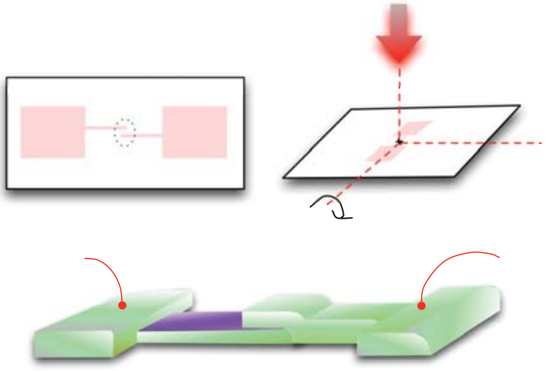

Figure 3.5. Process of fabricating tunnel junction. Blue color represents a thin layer of oxide

3.4 Bloch Oscillating transistor fabrications

BOT fabrication includes shadow evaporation at several angles. The narrow line width with large undercut requires different resist combination than described for previous structures. The details are presented in Appendix (Sec. 8.1). Here I briefly explain the process schematically.

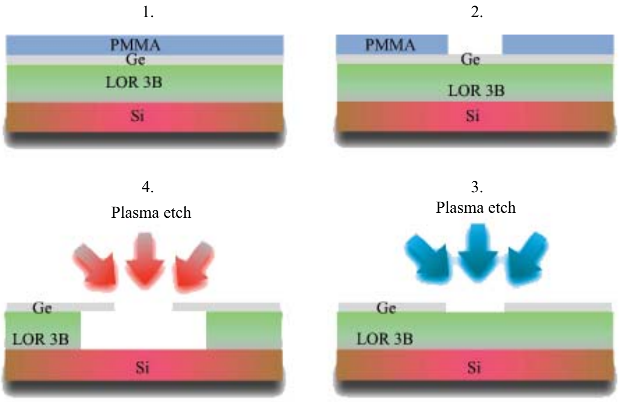

Figure 3.6. Schematic flow for the BOT fabrication process. The arrows indicate the etching.

After all the etching processes involved in Ge-mask fabrication (see Fig. 3.6), the substrates were ready for evaporation. The angles required for the evaporation were calculated by keeping in mind the thickness of the LOR. We can ignore the thickness of Ge in this case.

- -18^0 tilt for Cr (7 nm).
- -30^0 tilt for Al island (20 nm).
- $+45^0$ rotation along with $+30^0$ tilt for Al of thickness 30 nm for fork

- $+2^0$ tilt for Cu 40 nm

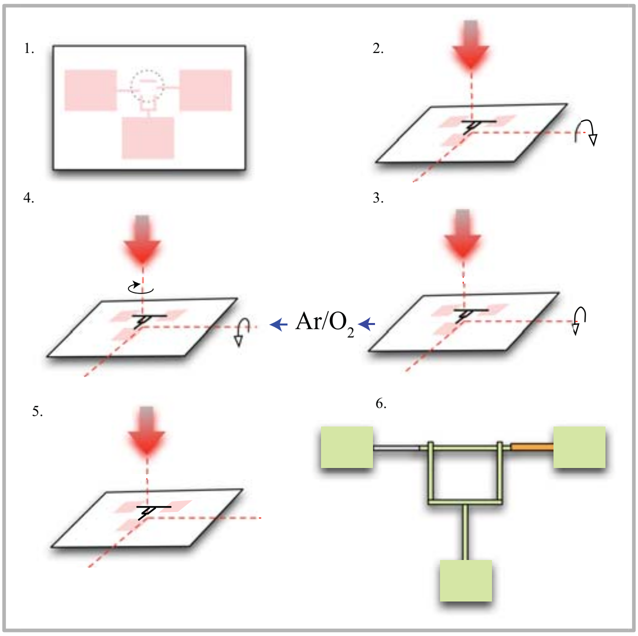

Figure 3.7. Evaporation scheme for the fabrication of BOT. The steps are explained in the text. Step 6 indicates the final product; the symbols JJ, B junction and C are explained in the caption of Fig. 3.8.

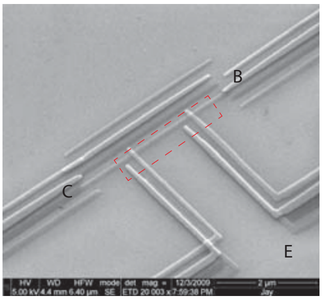

Figure 3.8. SEM image of a BOT. Emitter, Base and Collector are labeled as E, B and C respectively. Cr strip acts as the collector. The dashed rectangle is to highlight the two JJs (Al-oxide-Al) which are enclosed in a loop. This part forms the emitter. Base is formed by the NIS junction (Cu-oxide-Al).

An important point is that, to achieve a 100-nm line in the last evaporation step, the initial width has to be well above 100 nm, because in every evaporation step the window gets narrower due to metal piling up at the edges.

4. Cross-correlation experiments

The cross-correlation measurements described in this chapter were performed in a liquid helium cryostat at 4.2 K. The schematic of the employed setup is shown in Fig. 4.1. The noise generated from the sample is amplified by a low-noise amplifier located in helium bath close to the sample. The output of the low noise amplifier is further amplified by room temperature amplifiers. The setup features several DC and RF lines for the measurement. The measurement bandwidth is essentially limited by the circulator and the low noise amplifiers (LNA). The LNAs have a bandwidth of 600-950 MHz while the circulators operate over a 600-900 MHz band at room temperature. At 4.2 K, the usable bandwidth becomes 650-900 MHz (see Fig. 4.2). We used Cu coaxial for the connections from the sample to the circulator and the LNA stage as that provides the best signal transfer between these elements and all of them are immersed into the bath. Cabling from top of the cryostat to the LNA is done with stainless steel to reduce heat conduction to the bottom of the cryostat.

The DC lines are filtered first on top of the cryostat with Mini-Circuit SLP-1.9 low pass filters with a cut-off frequency at 1.9 MHz. Inside the cryostat twisted pairs are used to reduce cross talk. Further filtering is provided with a grounded copper tape around the twisted pairs which creates a lossy transmission line (tapeworm filter) at high frequencies. The filtering prohibits RF interference to the sample through the DC lines in the measurement band frequency.

4.1 HBT measurement results: cold electrons & hot electrons

To determine the HBT exchange correction factor we have performed three consecutive measurements, namely A, B and C, shown in left schematic of Fig. 2.8, respectively. The cross-correlation is measured in each configuration from

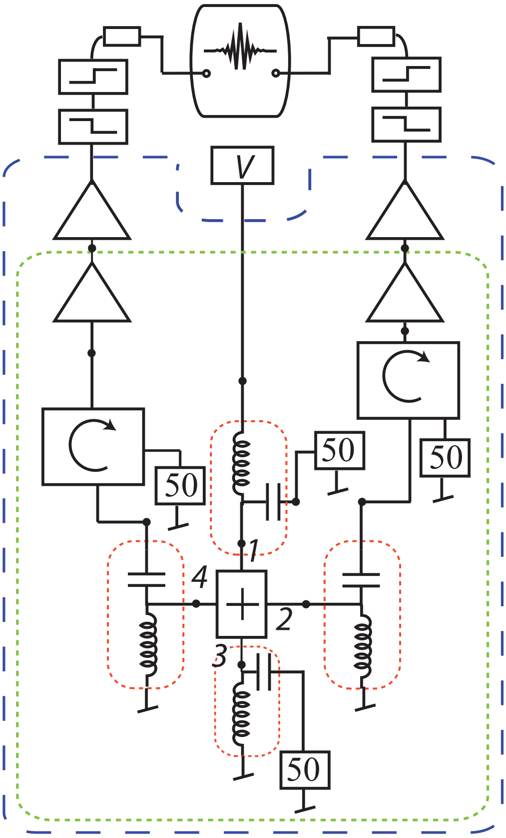

Figure 4.1. Schematic of the experimental set up to measure cross correlation. In this configuration 4 terminals of the sample are connected to bias-tees. The above schematic is for the case of S^A where the terminal 1 is biased through a bias-tee. The correlated spectra is detected from 2nd and 4th terminal. There are two circulators in these two lines which prohibits any back action noise coming from the amplifiers. DC end of the bias-tee is connected to the top of the cryostat which can be used to change the biasing corresponding to different measurement scheme. After the amplification by room temperature amplifiers signals are passed through (low and high pass) filters and fed into Lecroy oscilloscope.

the side terminals 2 and 4. In configuration A, bias is applied to terminal

Table 4.1. Sample parameters of the diffusive cross. l_a is the arm length and A denotes the central area of the cross.

Sample	Resistance of the arms (Ω)				l_a nm	A nm × nm
	arm1	arm 2	arm 3	arm 4		
#1	110	125	310	135	450	60 × 70
#2	40	42	36	45	475	150 × 130

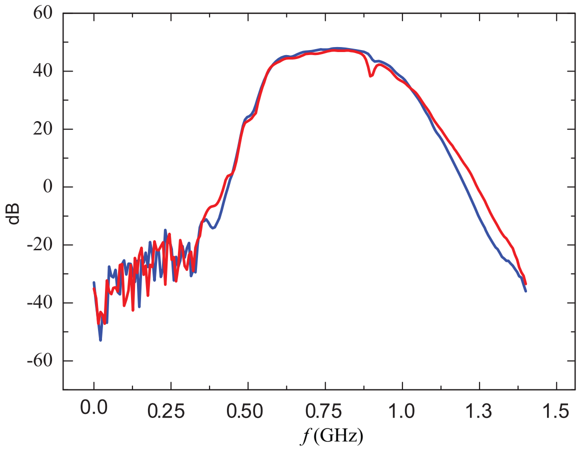

Figure 4.2. Overall bandwidth of the circulator and amplifiers in chain shows a 3 dB flat-band from 650 - 900 MHz.

1 while the other terminals are connected to DC ground. For case B, the connection is reversed so that the opposite terminal 3 is biased. The final measurement C is done with both contacts 1 and 3 biased simultaneously and rest DC grounded. The time traces of the fluctuations were recorded using Lecroy oscilloscope with two independent channel. For each biasing point, 100 pairs of time traces were collected and correlation result was calculated from summing up (averaging) the cross-correlations of each of these pairs. The sampling rate was 5 GS/s, i.e., slightly oversampled in order to secure the quality of the data. Each trace had 1 MS of data points and the overall cross-correlation sensitivity of our setup was 10 mK with 100 averaged traces.

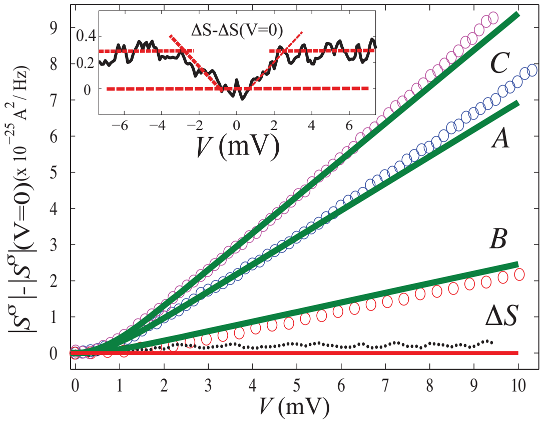

Figure 4.3. Cross-correlations $|S^\sigma| - |S^\sigma(V = 0)|$ of a four-terminal diffusive system (sample #1) in the non-interacting regime measured at low bias voltages.

The result $|S^\sigma| - |S^\sigma(V = 0)|$ obtained for the case of cold electron system is shown in Fig. 4.3 for sample # 1. The solid curves in the main picture show an excellent fit which is obtained from semiclassical theory [3]. Similar measurements for hot-electron system on sample #2 are shown in Fig. 4.5. The voltage range in the latter measurement is almost by a factor of 10 higher than that on sample #1.

In sample #1, we found that exchange correction $\Delta S(V) - \Delta S(V = 0)$ increases linearly till 2 mV, as seen in the inset of Fig. 4.3, above which it becomes nearly bias independent. Using all the shot noise data at different configurations, we found that the deviation from diffusive linear regime towards hot-electron regime starts around $\sim$ 6 mV. Nevertheless, sample #1 exchange correction factor shows sign of positive exchange effect $\Delta S = 0.02 S^C$ at small bias.

At $eV \gg k_B T$, the strength of the electron-electron interaction increases [30–32], which eventually drives the diffusive cross to quasi-equilibrium where the electron distribution tends towards a Fermi function. In the hot electron regime, the magnitude of shot noise is determined by the local non-equilibrium temperature distribution. Fig. 4.4 displays calculated temperature profiles for the different HBT biasing conditions A , B, and C, respectively. The picture displays the T-distribution vs. position x in the biasing leads and in one of the non-biased conductors. Non-equal currents in the biased conductor compared with the grounded leads produces asymmetric temperature distributions, where the profile in the individual arms follow the typical quadratic structure of the hot electron regime. The cross-correlation spectra in this case along with $\Delta S(V) - \Delta S(V = 0)|$ for sample #2 are displayed in Fig. 4.5. We see that $\Delta S - \Delta S(V = 0)$ decreases linearly with increasing bias ($\Delta S < 0$).

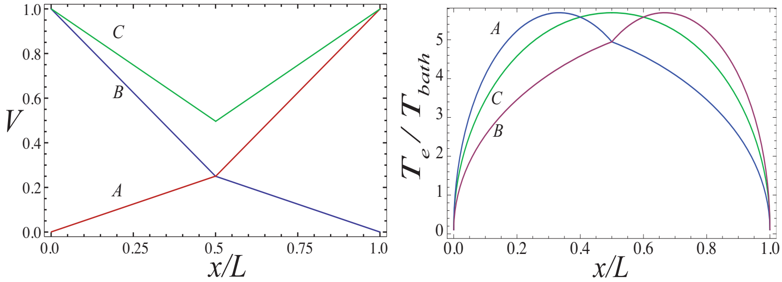

Figure 4.4. Potential profile of a symmetric diffusive cross in A, B, C configurations along with electron temperature profile in the case of hot-electron regime.

According to the condition $(\kappa_s/p_F)(eV)^2/\epsilon_F > D/L^2$ [31, 32] the strong interaction limit is satisfied for our data above 10 mV; here $\kappa_s = e^2\nu_F/\epsilon_0$ is the inverse screening parameter ($\simeq 1.5 k_F$ for Cu). Hence, at $\sim$ 10 mV the electron-electron interaction strength starts to increase and the system nearly reaches the pure hot-electron regime at the highest bias of 70 mV (Fig. 4.5) where F has increased by 15% from the non-interacting limit (see Publ. I).

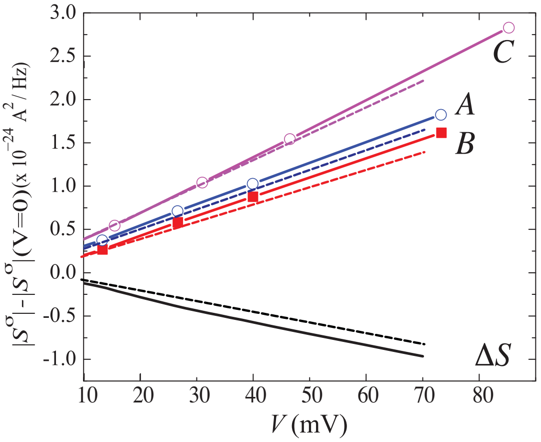

Figure 4.5. Cross-correlation results on sample #2 in interacting regime along with exchange term plotted with bias. The dotted line are obtained from simulation.

On sample #2, we observe no decrease in noise power with bias, which can be attributed to the fact that the phonon lattice overheats in the wire and thus the heat flow from electrons to the phonon system is not sufficient to alter the hot-electron temperature distribution governed by the electronic heat conduction. Therefore, we still see a rise in cross-correlated noise spectra at $V \gg 10$ mV when the electron system and the phonons heat up to $50-100$ K.

The hot-electron results of sample #2 are compared with the circuit theory model where the diffusive conductor is replaced by an array of tunnel junctions [33]. The simulation with non-relaxing nodes between junctions produces $F = 1/3$ for a two-terminal conductor while the use of nodes with scattering imposed Fermi distributions yields $F = \sqrt{3}/4$. The simulation where the asymmetry of the arms are also taken into account has been found to generate similar ΔS variation (Fig. 4.5).

4.2 HBT measurement on a tunnel junction cross

We have also made an HBT type of experiment on a tunnel junction cross system. Most notably we observed a distinct change in sign of ΔS in comparison to the diffusive cross system. The measurement configurations and techniques are similar as for the diffusive cross system described in the previous section

(Fig. 2.8) and the tunnel junction cross was also investigated at liquid helium temperature.

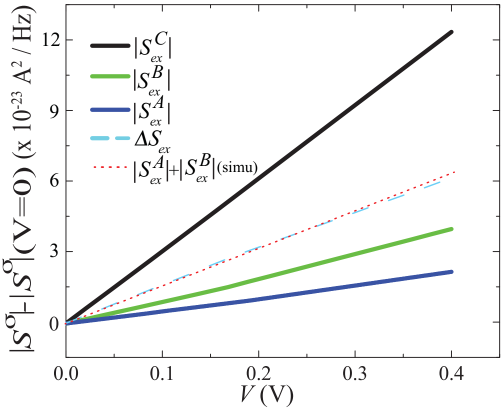

Figure 4.6. The measured $S^{\sigma} - S^{\sigma}(V = 0)$ and $\Delta S - \Delta S(V = 0)$ in a tunnel junction cross system along with simulation result (dotted lines).

We have employed circuit theory simulation to compare our results and the match with our experimental findings proved to be very good. The experimentally observed ΔS is practically identical to the $\Delta S_{ex} = |S^A_{ex}| + |S^B_{ex}|$ found from the simulation and is positive in sign. A comparison of the simulated cross correlation ratios with the experimental results is shown in Tab. 4.2. We also mention the simulation result in the hot electron case which clearly proves that the tunnel junction cross system was not in hot electron regime.

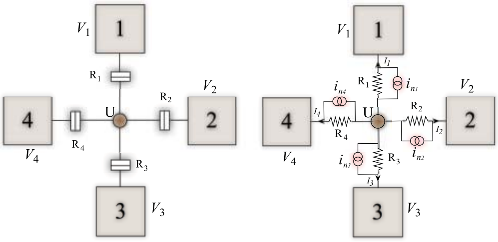

Figure 4.7. (a) Circuit model for tunnel junctions in cross formation. The central dot denotes an equilibrium node in the simulation. (b) The right figure is the classical model discussed by Langen et. al [34], showing independent noise sources in each arm.

The classical situation is discussed by Langen and Büttiker [34] as sketched in Fig. 4.7b where tunnel junction resistances are marked as the Rs and $i_m = 2e\langle I_m \rangle$ is the noise generated by the tunnel junctions. The resistances of the connecting conductors among the tunnel junctions are negligible compared to Rs. Naively, one could expect that the correlated noise in the A, B, C con-

Ratios	S^C/S^A	S^B/S^A	S^C/S^B
Experiment	5.4	1.80	2.9
Simulation	5.4	1.75	3.1
Simulation (hot)	2.2	1.2	1.8

Table 4.2. Comparison of the measured and the simulated excess cross correlations in terms of ratios of different biasing configurations A, B, and C for both interacting (hot) and non-interacting (cold) tunnel junction cross system.

figurations would fulfill, $S^C = S^A + S^B$ for a system of classical noise sources but it is not the case. The voltage fluctuations in the central region (around the mean voltage $U = \sum_k V_k/4$ are responsible for the current correlation among the leads which is given by

$$S_{kl} = e \sum_{m=1}^{4} [1 + 4(2\delta_{kl} - 1)(\delta_{mk} + \delta_{ml})] \frac{|V_m - U|}{8R} \tag{4.1}$$

in the case of a symmetric noise generator system with $R = R_1 = R_2 = R_3 = R_4$. For the symmetric case, $S^C/S^{A,B} = 4$ as follows from Eq 4.1. The TJ-cross sample measured has non-identical tunnel junction resistances which will modify the central potential as $U = (V_1/R_1 + V_2/R_2 + V_3/R_3 + V_4/R_4)/(R_1 + 1/R_2 + 1/R_3 + 1/R_4)$, which, in turn, will influence the ratios of cross-correlation powers, $S^C/S^{A,B}$. Nevertheless, the sign of exchange correction factor $\Delta S = |S^C| - |S^A| - |S^B|$ will remain positive irrespective of the arm resistances.

In a diffusive cross system in the semiclassical (dephased cold electron) regime, $|S^C| - |S^A| - |S^B|$ does not change with bias. In the hot electron regime, when electron-electron interaction dominates, the sign of $|S^C| - |S^A| - |S^B|$ is opposite than in the case for a tunnel junction cross system.

4.3 Prerequisites for the correlation study on diffusive conductors

4.3.1 Different length scales in diffusive conductors

Length of a diffusive system is an important factor when aiming to observe shot noise. But this length alone is not the fundamental factor. The behavior depends on several other scales like electron-phonon length (l_{el-ph}), electron-electron interaction length (l_{el-el}), phase-breaking length (l_φ) which have been collected to Tabl. 4.3 below along with descriptions of the charge transport and the conserved quantities in the transport.

Limit	Length	Conserved quantity
Ballistic	$L \ll l_{el}, l_{e-e}, l_{e-ph}$	current for each momentum state
Diffusive	$l_{el} \ll L \ll l_{e-e}, l_{e-ph}$	current for each energy
Quasi-equilibrium	$l_{el}, l_{e-e} \ll L \ll l_{e-ph}$	charge and energy currents
Local equilibrium	$l_{el}, l_{e-e}, l_{e-ph} \ll L$	charge current

Table 4.3. Different length scales and the corresponding regimes in a mesoscopic conductor [35].

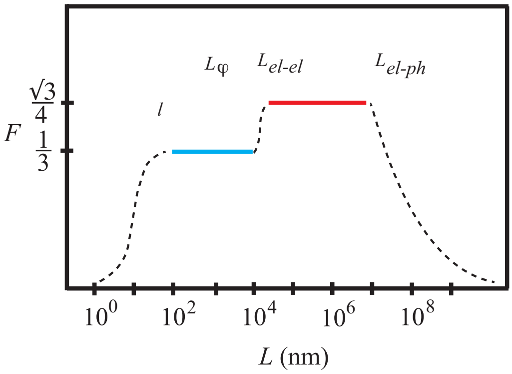

Figure 4.8. Dependence of Fano factor on the length scale in a metallic conductor with impurities [36].

4.3.2 Dependence of Fano factor on temperature

Phonons are excited lattice vibration modes. The collisions between electrons and phonons are inelastic which result in dephasing of electron motion. With a reduction in temperature the available phonon modes to absorb or emit decrease resulting in a simultaneous decrease in the dephasing rate of electrons. Usually the dephasing length can be in microns at liquid helium temperature in a disordered metal and can be even longer in high mobility semiconductors. The structure of the system in comparison to the dephasing length scale determines the dimensionality of the system in regard to quantum-interference effects. In weakly disordered conductor ($L_\varphi < L_x, L_y, L_z$) electron-phonon scattering is the main dominant inelastic dephasing process. At low temperature and low voltage, the optical phonons can be neglected and it is sufficient to consider only the acoustic phonons.

When the sample length is smaller than the inelastic length scales, l_{el-el}, l_{el-ph} the Fano factor of a diffusive conductor turns out to be $1/3$. But the effect of electron-electron and electron-phonon interaction affects the Fano factor. The dependence of Fano factor on the interaction length scales is shown in Fig.

4.8.

We estimate the dependence of F on temperature using Ref. [37]. The heat balance equation which depends on the phonon dimensionality has the form of

$$\varepsilon_{inel} = \Sigma(T^{\alpha+3} - T_{ph}^{\alpha+3}) \tag{4.2}$$

where α depends on dimensionality. For a 3-dimensional system, $\alpha = 2$ and the above equation displays T^5 dependence. For a 2-dimensional system, the exponent is $\alpha + 3 = 4$. We estimate the temperature dependence of Fano factor from the relation $F \propto V^{\frac{\alpha+1}{\alpha+3}}$ [37] that

$$F \propto T^{\frac{\alpha+1}{\alpha+3}}. \tag{4.3}$$

This leads to the conclusion that $F \propto T^{-0.5}$ in two dimensions [1]. Our measurement of shot noise at different temperatures performed on a two-terminal diffusive wire follows the above relation. The experimental data are presented in the following section.

4.3.3 Shot noise measurement scheme

The setup used for shot noise measurements shown in Fig. 4.9 is similar to the one used for cross-correlation measurements and presented earlier in Fig. 4.1. Instead of recording the time traces with an oscilloscope we have employed an RF-diode [41] to detect the noise power (see Fig. 4.9).

Shot noise vs. bias current is depicted in Fig. 4.10 at different temperatures between 4.2 – 18 K. The lowest trace represents the data measured at 4.2 K. Overall, the noise power increases with increasing temperature. Fano factors obtained from the fits are plotted with temperature in Fig. 4.10b. The straight line is a fit to the data on log-log scale with the slope of -0.5.

---

[1] Refs. [38] and [39] give a relation of Fano factor with $\beta = L/l_{el-ph}$ for 3-dimensional system.

$$\begin{aligned} \frac{S_I}{2eI} = F = & \tfrac{1.2}{\beta^{2/5}}, \quad \frac{L}{l_{el-el}} << 1 \\ = & \tfrac{1.05}{\beta^{2/5}}, \quad \frac{L}{l_{el-el}} >> 1 \end{aligned} \tag{4.4}$$

The factor 5 in the denominator of the exponent comes from dimensionality which is 3-dim in this case. For 2-dim, or for disordered case with $\tau_{el-ph} \propto 1/T^2$ [40] this exponent becomes 4 which also leads to the conclusion that from Eq. 4.4 we can approximate the functional dependence of F on T:

$$F \sim \frac{1}{\beta^{2/4}} \sim \frac{l_{el-ph}^{2/4}}{L^{2/4}} = \frac{(D\tau_{el-ph})^{1/4}}{L^{2/4}} \propto T^{-2/4} \propto T^{-0.5}. \tag{4.5}$$

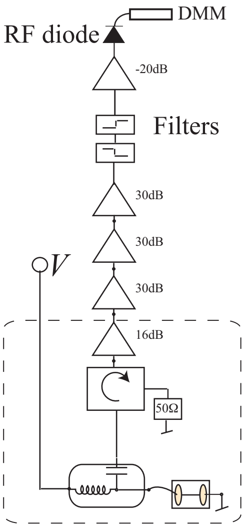

Figure 4.9. Schematic of the measurement set up for shot noise measurement of a two-terminal diffusive wire using RF-diode detection. The region inside the dashed box is at liquid helium temperature.

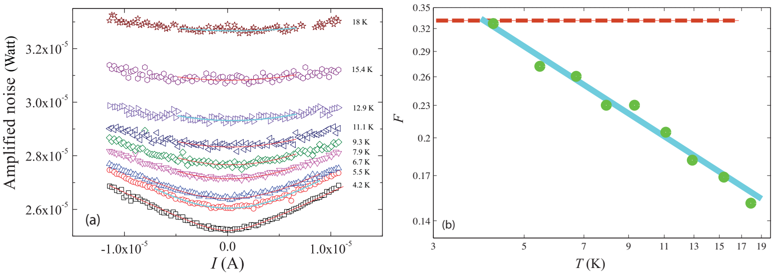

Figure 4.10. (a) The measured shot noise power of a biased two-terminal diffusive wire plotted vs. current at different temperatures. (b) Fano factor determined from the results of (a) is plotted vs. temperature. Dashed line marks the Fano factor 1/3 for diffusive system.

The effect of electron-electron interaction can be neglected in our considerations. From the estimates of $\tau_{el-el}^{-1} = k_B T \frac{e^2 R_\square}{2\pi\hbar^2} \ln\left(\frac{\pi\hbar}{e^2 R_\square}\right)$ using Altshuler formula, l_{el-el} drops from 1.2 μm to 0.97 μm over the temperature range from 4.2 K to 18 K. So at the highest temperature measured $L \sim l_{el-el}$, and the electron-electron interaction will not influence the shot noise power much. The strong inelastic collision due to electron-phonon interaction will dominate the decrease of the Fano factor.

5. Mesoscopic superconductivity

5.1 Introduction

Superconductivity encompasses a plethora of interesting phenomena that become even more intriguing at small length scales. In 1957, Bardeen Cooper and Schrieffer presented the microscopic theory (BCS theory) for superconductivity [42]. This theory provided and explanation of pairing of electrons to form Cooper pairs which essentially explains the superconductivity. These two electrons, bound by weak attraction via electron-phonon interaction, can spread over a considerable distance and a macroscopic number of pairs can occupy the same region of space at the same time [43]. Another model addressing the issue of superconductivity is the Ginzburg and Landau model (GL) which is based on a phenomenological order parameter. The superconducting state can be described by a single wave function

$$\Psi(\mathbf{r}, t) = \sqrt{n_s(\mathbf{r})} e^{i\varphi(\mathbf{r})} \tag{5.1}$$

where n_s is proportional to the density of Cooper pairs and $\varphi(\mathbf{r})$ is the phase of the wave function. All the Cooper pairs in a superconductor have the same energy. This is referred to the ground state of the superconductor, and to excite this state, a finite energy must be supplied. The finite energy difference between the ground state and the excited state per particle is called the energy gap and denoted by Δ. The basic excitation of the system can be described as a breakup of a Cooper pair, and the energy needed for such an operation is 2Δ, which is the so-called pair binding energy. GL model is the limiting case of the microscopic BCS theory, and it is valid near T_C where T_C is the superconducting transition temperature. The superconducting energy gap Δ is given by $3.07k_B(T_C - T)^{1/2}$ when $1 - T/T_C \ll 1$.

In 1962 B. D. Josephson predicted the Josephson effect [44] which opened a new door for physicists and engineers to realize intriguing quantum phenomena in solid systems. According to his prediction, zero voltage supercurrent $I_S = I_C \sin\varphi$ flows between two superconducting electrodes separated by insulating barrier, where $\varphi = \varphi_1 - \varphi_2$ is the phase difference over the barrier. The critical current I_C is related to the Josephson energy E_J by $E_J = \frac{\hbar I_C}{2e}$. For a superconducting tunnel junction, i.e. Josephson junction (JJ), the critical current can also be determined from the normal state resistance R_n and Δ through the Ambegaokar-Baratoff relation $I_C = \frac{\pi\Delta}{2eR_n}$ [45]. The realization of JJs has revealed many aspects of quantum physics on macroscopic scale and such components have long been considered as potential building blocks for future quantum computers.

A current biased JJ can be modeled as a parallel combination of a capacitor, a resistor and an ideal tunnel element, a combination which is known as the resistively and capacitively shunted superconducting junction (RCSJ). A schematic circuit of a current biased JJ based in the RCSJ model is shown in Fig. 5.1.

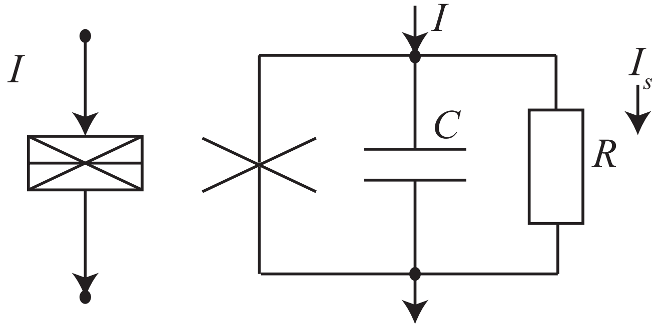

Figure 5.1. Josephson junction equivalent in RCSJ model with three parallel elements.

From the RCSJ model the time dependence of φ is implicitly governed by the Kirchoff's law

$$I = I_C \sin(\varphi) + I_S + C\frac{dV}{dt}, \tag{5.2}$$

which in terms of φ can be written as a second order differential equation

$$\frac{d^2\varphi}{d\tau^2} + \frac{1}{\omega_p RC}\frac{d\varphi}{d\tau} + \sin\varphi = \frac{I}{I_C}, \tag{5.3}$$

where $\omega_p = \sqrt{\frac{2eI_C}{\hbar C}}$ is the plasma frequency of the JJ and $\tau = \omega_p t$. The damping parameter in this form is given by $1/\omega_p RC$.

The junction dynamics can be well explained with Eq. 5.3 whose solutions can be obtained from the 'tilted washboard potential':

$$U(\varphi, t) = -E_J \cos\varphi - \frac{\hbar I}{2e}\varphi \tag{5.4}$$

The functional form of the washboard potential is illustrated in Fig. 5.2. The tilting of the washboard potential grows with the increase in the bias

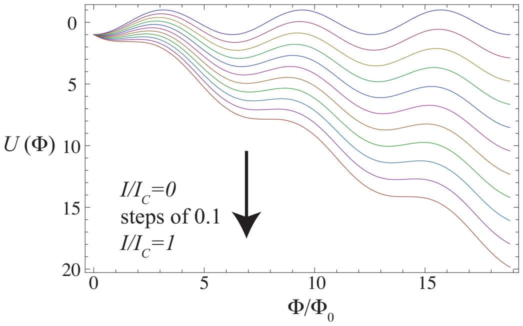

Figure 5.2. Washboard potential $U(\varphi)$ as function of φ showing the tilt with increasing I.

current I. The amplitude of the sinusoid is $E_J = \frac{\Phi_0 I_C}{2\pi}$. The dynamics can be thought of as an equation of motion of a particle with mass $(\hbar/2e)^2C$ at position φ in the "washboard potential", $U(\varphi)$. The sinusoidal dependence of washboard potential is responsible for JJ's ability to act as a non-linear inductor in modeling of the JJ-based devices such as superconducting quantum interference devices (SQUID) etc.

For an overdamped junction $\omega_p RC \ll 1$, Eq. 5.3 can be reduced to a first order differential equation

$$\frac{d\varphi}{dt} = \frac{2eI_C R}{\hbar}\left(\frac{I}{I_C} - \sin\varphi\right). \tag{5.5}$$

Integrating the above equation gives the expression of current-voltage relationship of an overdamped JJ:

$$V = R\sqrt{(I^2 - I_C^2)}. \tag{5.6}$$

The comparison of Eq. 5.6 with a linear, resistive $I - V$ curve is illustrated in Fig. 5.3, which shows that well above I_C the current-voltage relationship follows Ohm's law.

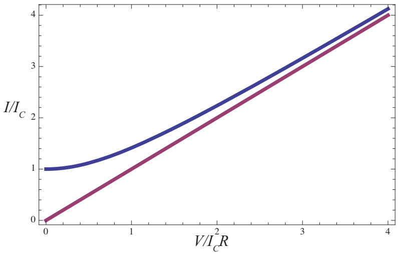

Figure 5.3. $I - V$ of a classical, overdamped Josephson junction compared with a linear (ohmic) $I - V$.

For an underdamped junction ($\omega_p RC > 1$), the voltage V remains zero until $I = I_C$. Above I_C the system jumps to a finite voltage state, the 'running state' in which φ increases at the rate of $\frac{2eV}{\hbar}$. In an ideal JJ at $T \ll T_C$, this running state occurs at $V = 2\Delta/e$. Another important feature of an underdamped JJ is its hysteretic $I-V$ curve.

JJ based devices which have been addressed in this thesis work are in the form of SQUID. A SQUID is a device consisting of JJs (or weak links) connected to each other in a form of a loop. If in a two-junction SQUID if individual JJs have equal I_C the total critical current can be written as

$$I_{SQ} = 2I_C \cos\left(\frac{\pi\Phi}{\Phi_0}\right) \tag{5.7}$$

where Φ is the flux enclosed by the loop. A double junction SQUID can be approximated as a single JJ with an effective E_J which depends on the individual $E_{J(1,2)}$s and the enclosed flux. The extra important freedom that a SQUID gives over a single JJ is the possibility to vary the E_J using external flux.

In classical JJs, the quantum uncertainty relation $\Delta N \Delta\varphi \geq 1/2h$ between the number of Cooper pairs and the phase of the superconductor does not play a role in determining the dynamics. In the case of small-capacitance Josephson junctions in a high impedance environment, the phase is no longer well defined due to quantum fluctuations. In this situation, the charge on the junction capacitance behaves as the quantum variable with good quantum numbers, and a description of the dynamics of the junction works in the reference frame of (quasi) charge [46, 47]. To explain central features of nano-scale junctions a quantum mechanical treatment of both variables φ and charge Q is needed. Quantum mechanically these variables form a pair of conjugate operators $\hat{Q}, \hat{\varphi}$ for which $\hat{Q}$ is canonically conjugate to $\hat{\varphi}$ with the commutation relation $[\hat{\varphi}, \hat{Q}] = 2ei$. The Hamiltonian takes the form

$$H = -E_J \cos\varphi - 4E_C \frac{\partial^2}{\partial\varphi^2}, \tag{5.8}$$

where $E_C = e^2/2C$ is the charging energy for a single electron charge. This Hamiltonian neglects the quasiparticle degrees of freedom. The solutions of Eq. 5.8 are of the form $\psi_q = u(\varphi)e^{iq\varphi}$ where 'q' is the quasicharge and $u(\varphi)$ is periodic with period 2π.

The energy eigenvalues can be classified in terms of quasicharge q, which is analogous to the crystal momentum in solid state physics [48]. The resulting band structure $E_n(q)$ looks similar to the Bloch bands in solid state periodic potentials. Thus, the main difference with the classical case is that the state of the junction cannot be described with a single value for φ but rather a distribution of φ has to be defined - this distribution may even be delocalized (i.e, Coulomb blockade of supercurrent).

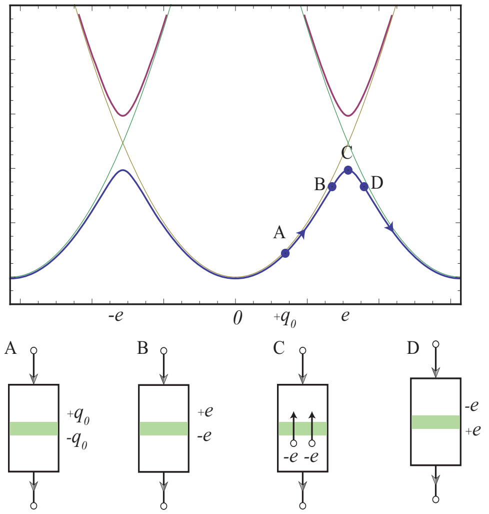

Figure 5.4. Band diagram and corresponding junction states at various points of lower energy band (adapted from Ref. [49]).

5.2 Bloch band dynamics

The energy levels $E_n(q)$ are energy bands with periodicity $2e$, since the first Brillouin zone extends over $-e$ to e. As shown in Fig. 5.4, the form of the energy bands is determined by the ratio between the two energy scales E_J and E_C [49]. The quasicharge dynamics of a small capacitance JJ in a high impedance environment is discussed elaborately in Ref. [49]. By inspecting Fig. 5.4, we end up with the following understanding of the dynamics of the junction. When the junction is biased with current less than Zener current, $I \ll I_z = \frac{\pi e E_J^2}{8\hbar E_C}$, the quasicharge increases upto $q = e$ and returns to $q = -e$ and back again to $q = e$. Thus, there is a coherent oscillation of quasicharge, i.e., Bloch oscillation. The junction state at each step is schematically described in Fig. 5.4. At the Brillouin zone boundary the Zener tunneling to second band is possible. The probability of transition from band $n-1$ to band n is given by

$$P^Z_{n-1\to n} \approx \exp\left(-\frac{\pi}{8}\frac{1}{n^{2n-1}}\left(\frac{E_J}{E_C}\right)^{2n}\frac{eE_C}{\hbar I}\right). \tag{5.9}$$

Apart from this mechanism, the actual downward and upward transition rates can be dependent on other factors when the junction is embedded in an environment. Zaikin and Golubev [50] have calculated the upward and downward transition rates Γ of a voltage biased JJ in a resistive environment (R_C) in the limit of $E_C \gg E_J$:

$$\Gamma_\uparrow = \frac{v}{2\tau}\exp\left\{-\frac{v_Z}{v-1}\left[1+\frac{\langle\delta q^2/e^2\rangle}{(v-1)^2}\right]\right\}, \tag{5.10}$$

while the down relaxation rate due to charge fluctuations is given by

$$\Gamma_{in\downarrow} = \frac{v_Z}{\tau\sqrt{2\pi\left\langle \delta q^2/e^2\right\rangle}} \exp\left\{-\frac{(v-1)^2}{2\left\langle \delta q^2/e^2\right\rangle}\right\}, \tag{5.11}$$

where $v = CV_C/e$, $\tau = R_C C$, $\langle \delta q^2 \rangle = k_B CT$, and

$$v_Z = \frac{\pi^2 R_C}{8R_Q}\left(\frac{E_J}{E_C}\right)^2. \tag{5.12}$$

The voltage v_Z is related to the so called Zener break down current by $I_Z = ev_Z/(4\tau)$. $R_Q = \frac{h}{4e^2}$ is the quantum resistance for Cooper pairs.

5.3 Environment and $P(E)$ theory

The transition rates in Eqs. 5.10 and 5.11 have been employed in Publ. III to model the dynamics of the JJ-based devices. The equation of the transition rates indicates that the environment plays an important factor in the band dynamics, and thus affects the $I-V$ characteristics of a tunnel junction. In order to calculate the $I-V$ characteristic of a normal metal (superconducting) tunnel junction, one needs to calculate the electron (Cooper pair) tunneling rate across the junction by taking the bias voltage into account.

For an isolated tunnel junction the energy before and after a single electron tunneling differs by E_C. This view is called the local view as the interaction of junction with the environment is ignored [51]. In the global view, the junction and the environment are considered together to evaluate changes in energy. In a voltage biased junction, the charge equilibrium is established immediately after the tunneling process, which is not the case for a current biased junction.

The classical relaxation of charge in a circuit can be described in terms of the impedance seen by the current. The impedance can be decomposed into an infinite number of LC oscillators. The quantum mechanical treatment of an LC circuit is the basis of the phase fluctuation a.k.a. $P(E)$ theory where the electromagnetic environment is considered as an ensemble of harmonic oscillators. Introducing the phase in the case of Cooper pairs,

$$\varphi(t) = \frac{2e}{\hbar}\int_{-\infty}^{t} dt' U(t') \tag{5.13}$$

the Hamiltonian of the system is given by,

$$H = \frac{Q^2}{2C} + \frac{1}{2L}\left(\frac{\hbar}{2e}\right)^2\left(\varphi - \frac{2e}{\hbar}Vt\right)^2. \tag{5.14}$$

where, $Q = CV$ is the average charge on the capacitor. Eq. 5.13 is essentially the Josephson relation. The above Hamiltonian shows that the average phase varies with time as $\varphi(t) = 2e/\hbar Vt$.

The fluctuations around the mean value can be written as[51]

$$\tilde{Q}(t) = Q(t) - CV, \tag{5.15}$$

$$\tilde{\varphi}(t) = \varphi(t) - \frac{2e}{\hbar}Vt, \tag{5.16}$$

where the fluctuating variables $\tilde{Q}$ and $\tilde{\varphi}$ satisfy the commutation relation $[\tilde{\varphi}, \tilde{Q}] = i2e$.

Thus, in rotating reference frame the above Hamiltonian, (Eq. 5.14) can be expressed as

$$H = \frac{\tilde{Q}}{2C} + \frac{1}{2L}\left(\frac{\hbar}{e}\tilde{\varphi}\right)^2. \tag{5.17}$$

This Hamiltonian shows the similarity between the LC- circuit and a harmonic oscillator. When an electromagnetic environment is considered as an ensemble of LC oscillators the Hamiltonian for the environment can be written as a summation of LC oscillator Hamiltonians

$$H_{env} = \frac{\tilde{Q}^2}{2C} + \sum_{n=1}^{\infty}\left[\frac{q_n^2}{2C_n} + \left(\frac{\hbar}{2e}\right)^2 + \frac{1}{2L_n}(\tilde{\varphi} - \varphi_n)^2\right] \tag{5.18}$$

with an appropriate density that corresponds to the Ohmic dissipation [51].

5.3.1 Electromagnetic environment

In the previous section I showed the resemblance of the environment with an ensemble of electric oscillators. Now it is time to discuss briefly the influence of electromagnetic environment in Cooper pair tunneling. Consider a Josephson junction biased through a resistor R by voltage V. The Hamiltonian of the system can be written as

$$H = H_J + H_{env}, \tag{5.19}$$

where H_J represents the Josephson coupling contribution while H_{env} includes all other electrical elements in the circuit.

The above Hamiltonian is the basis for understanding the dynamics of the JJ. The tunneling rates can be calculated by means of the Fermi golden rule:

$$\Gamma_{i\to f} = \frac{2\pi}{\hbar}|\langle f| H_J |i\rangle|^2\delta(E_i - E_f), \tag{5.20}$$

where $\langle f| H_J |i\rangle$ is the matrix element describing the transition, while E_i and E_f correspond to the energies of these initial and final states. By summing over all possible initial and final states, the tunneling rate becomes

$$\Gamma(V) = \frac{2\pi}{\hbar}\sum_{f,i}|\langle f| H_J |i\rangle|^2 P(i)\delta(E_i - E_f), \tag{5.21}$$

where $P(i)$ is the probability of finding the system initially at state i [51].

If the environment is in thermal equilibrium the forward tunneling rate becomes

$$\Gamma(V) = \frac{\pi E_J^2}{2\hbar} P(2eV), \tag{5.22}$$

where $P(E)$ is the Fourier transform of the phase-phase correlation function $\langle e^{i\varphi(t)} e^{i\varphi(0)} \rangle$ given by

$$P(E) = \frac{1}{2\pi\hbar} \int_{-\infty}^{\infty} dt \exp\left[J(t) + \frac{i}{\hbar} Et\right]. \tag{5.23}$$

and where $J(t)$ for a linear environment is given by

$$J(t) = 2\int_{-\infty}^{\infty} \frac{d\omega}{\omega} \frac{ReZ(\omega)}{R_Q} \frac{e^{-i\omega t} - 1}{1 - e^{-\hbar\omega/(2k_B T)}}, \tag{5.24}$$

$P(E)$ essentially describes the probability of energy exchange between the tunneling electron with its environment. The main features of $P(E)$ are,

$$\int_{-\infty}^{\infty} dEP(E) = e^{J(0)} = 1 \tag{5.25}$$

$$\int_{-\infty}^{\infty} dEEP(E) = i\hbar J'(0) = E_C. \tag{5.26}$$

For an ohmic shunt R, the environmental $Z(\omega) = (\frac{1}{R} + i\omega C)^{-1}$ where C is the junction capacitance. Thus,

$$Re\{Z(\omega)\} = \frac{R}{1 + (\omega RC)^2}. \tag{5.27}$$

At low temperatures $P(+2eV) \gg P(-2eV)$, which reduces the $I - V$ to the form

$$I(V) = \frac{\pi e E_J^2}{\hbar} P(2eV). \tag{5.28}$$

The $P(E)$ function is strongly peaked at E_C in a highly resistive environment $R \gg R_Q$. We can approximate it as a Gaussian function of the form,

$$P(E) = \frac{1}{\sqrt{4\pi E_C k_B T}} \exp\left[-\frac{(E - E_C)^2}{4E_C k_B T}\right], \tag{5.29}$$

where $E_C = (2e)^2/2C$ corresponds to the Coulomb energy of the Cooper pair. The width of the peak is governed by the thermal noise of resistance R. An $I - V$ calculated using the $P(E)$ function in the limit $R/R_Q \gg 1$ is plotted in Fig. 5.5.

5.4 Josephson inductance

The quantum mechanical properties of φ have been reviewed in several articles [47, 52]. following RCSJ model I already derived earlier that total current in a current-biased JJ is given by

$$i(t) = I_C \sin\varphi(t) + \frac{v(t)}{R} + C\frac{d}{dt}v(t). \tag{5.30}$$

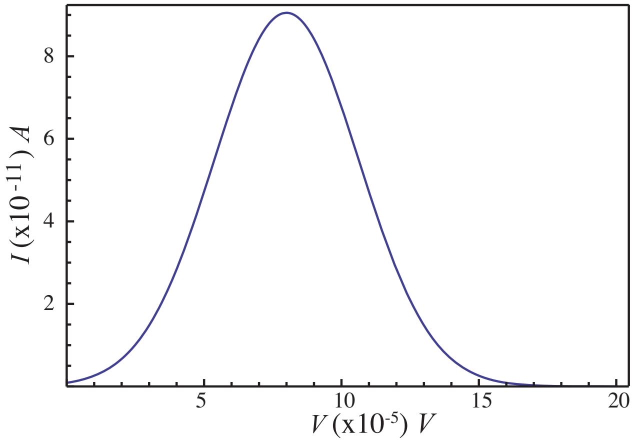

Figure 5.5. $I-V$ calculated using Eqs. 5.28 and 5.29 in the limit of high impedance environment. The parameters are of an actual measurement presented in Publ. III where E_C=40 μeV, E_J=3.5 μeV, T=90 mK.

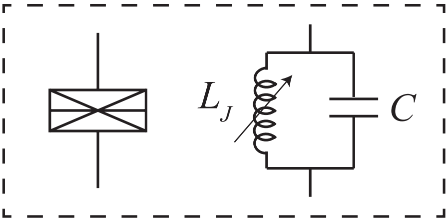

Figure 5.6. Josephson junction can be modeled by the parallel combination of a capacitor C and a tunable nonlinear inductor L_J.

Taking the time derivative of the above equation yields

$$\frac{d}{dt}i(t) = \left[\frac{2\pi I_C}{\Phi_0}\cos\varphi(t)\right]v(t), \tag{5.31}$$

which shows that the time derivative of Josephson current is proportional to voltage. The proportionality factor corresponds to an inductance $L_J = \frac{\Phi_o}{2\pi I_C \cos\varphi}$, where the cosine term is responsible for the non-linearity of the inductance. Josephson inductance L_J can also be defined in terms of the energy as

$$L_J = \frac{\Phi_0}{2\pi}\left(\frac{\partial^2 E}{\partial \varphi^2}\right)^{-1}. \tag{5.32}$$

Thus, a JJ is a non-linear inductor which forms together with the junction capacitance an anharmonic oscillator with discrete and non-equally spaced energy levels [53].

The formulation of L_J can also be extended to the Cooper pair transistor which comprises of two JJs and an island coupled to a gate (see Fig. 5.7). Introducing a variable d for the asymmetry of the junctions, the potential

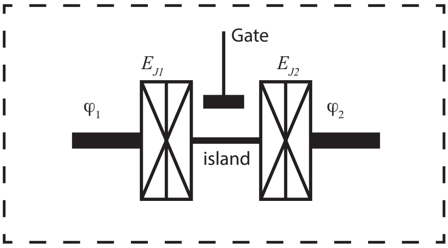

Figure 5.7. Schematic of a single Cooper pair transistor (SCPT) consisting of two JJs and an superconducting island in between.

energy of the system can be written as,

$$V = -E_J(1-d)\cos\varphi_1 - E_J(1+d)\cos\varphi_2. \tag{5.33}$$

Introducing a new set of variables [54] $\varphi = \varphi_1 + \varphi_2$ and $\theta = (\varphi_1 - \varphi_2)/2$ the full Hamiltonian of such a system can be written as

$$H = E_C(n-n_g)^2 - 2E_J\cos\frac{\varphi}{2}\cos\theta + 2dE_J\sin\frac{\varphi}{2}\sin\theta - \frac{1}{2}C_gV_g^2, \tag{5.34}$$

where $E_C = e^2/2C_\Sigma$ is the charging energy of the island. Total capacitance of the island is given by $C_\Sigma = C_1 + C_2 + C_g$, n is the count of the Cooper pairs on the island, and $n_g = C_gV_g/e$ is the gate-voltage-induced charge on the island. Eq. 5.34 specifies the eigenenergies $E_i(\varphi, n_g)$ of the SCPT, which in turn yield the Josephson inductance.

Considering two charge states, we obtain for the Josephson inductance (L_J) of a superconducting SET in ground state to take the form

$$L_J = \pm\left(\frac{\Phi_0}{2\pi}\right)^2 \frac{8\sqrt{2}}{E_J} \frac{\left[1+\frac{8}{x^2}(1-n_g)^2+\cos\varphi\right]^{3/2}}{\left[4+\frac{32}{x^2}(1-n_g)^2\right]\cos\varphi + 3 + \cos 2\varphi}, \tag{5.35}$$

where $x = E_J/E_C$ and + and - sign correspond to the ground and excited states, respectively. Determination of L_J provides a means to determine the current-phase relation of a SCPT through the relationships

$$L_J^{-1} = \frac{\partial I}{\partial \Phi}, \tag{5.36}$$

$$I(\varphi) = \frac{\Phi_0}{2\pi}\int_0^{\varphi} L_J^{-1} d\varphi. \tag{5.37}$$

For a tunnel barrier with $T_n \ll 1$, the current-phase relationship is sinusoidal which leads to fact that $L_J^{-1} \propto \cos\varphi$ (see Eq 5.31).

5.5 Superconducting artificial molecules

The term 'artificial' atom or molecule emerges with a meaning different from the usual in this context. The atoms and molecules are not in true sense atomic and molecular in size but their distinct features (energy levels) are of interest to us. No more elements are being added in the periodic table. Originally, the idea of 'quasiatom' made of semiconductor heterostructures was proposed with controlled 3-dim doping which could show well-defined wave functions under certain conditions [55]. Realizing the atomic features came however, through another way, 2-dim patterned systems . A brief review on the concept of an artificial atom is presented in Ref. [56]. In true sense, single electron transistors, quantum dots and zero-dimensional electron gases are artificial atoms. Like natural atoms, these structures also contain a discrete number of electrons and have discrete energy levels. Our work on an artificial molecule is not based on semiconductor heterostructures, but instead we have implemented a JJ based structure to demonstrate artificial 'molecule' kind of behavior.

Let's consider a diatomic molecule consisting of two atoms. As the molecule contains two atomic nuclei, we have two extra degrees of freedom in comparison to a single atom. The nuclei can vibrate with respect to an equilibrium separation in addition to the rotational motion around a fixed axis. The electronic motion is much faster than atomic motion. The wavefunction of the molecule can be written as $\Psi = |\Psi_e\rangle\,|\Psi_n\rangle$. The nuclear part can further be considered to consists of a vibrational and rotational terms $\Psi_n = |\Psi_v\rangle\,|\Psi_r\rangle$. Vibrational states can be approximated to be the states of a simple harmonic oscillator.

The spectroscopy of a diatomic molecule is based on observing of electromagnetic-field-induced transitions between states with different quantum numbers. The main interest is to observe the intensity of the transitions where the rotational state does not change. The simultaneous transitions of vibrational and electronic states are called vibronic.

From Fig. 5.8 demonstrates the vibronic transitions in a diatomic molecule. There are two nearly parabolic vibrational potentials corresponding to different equilibrium distance between the nuclei. The vertical arrow denotes the transitions between two states. The most intense transitions occur when the overlap integral $\int < \psi'_{v'}|\psi_v >$ between vibrational states in different electronic states has a maximum. This is called as Franck-Condon principle [57, 58].

In Publ. V, we deal with an artificial molecule that, in addition to electronic states, also includes the analog of nuclear vibrations present in a diatomic molecule. In our case, the electronic states of the molecule are represented by a Josephson-junction qubit, and the nuclear separation corresponds to the magnetic flux in a loop containing the qubit. A detailed discussion about

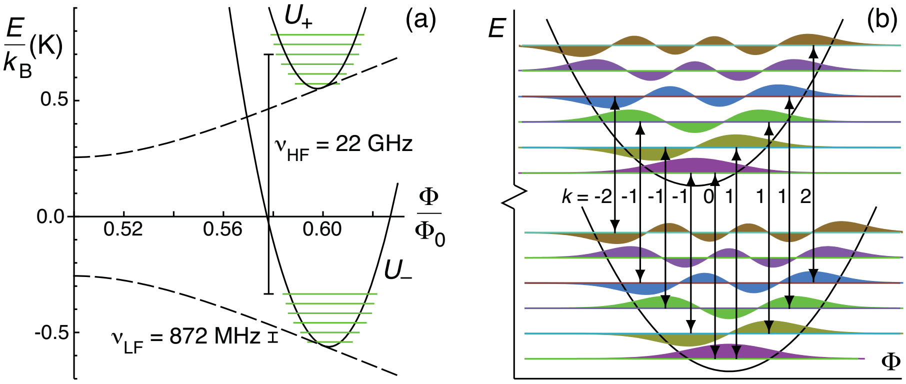

Figure 5.8. Potential energy and energy eigenstates of an artificial molecule. The arrows show the possible transition following Franck-Condon principle. k denotes the change in vibrational quanta (adapted from Publ. V).

vibronic transition related to Publ. V can be found in Ref. [59].

The potentials in our artificial molecule are illustrated in Fig. 5.8. The two states of the qubit correspond to two electronic states in a molecule. For both, there are several vibrational states.

The two electronic states of the artificial molecule are represented by

$$E^q_{\pm} = \pm\frac{1}{2}\sqrt{E^2_{el} + E_{J0}\cos^2(\pi\Phi/\Phi_0)} \tag{5.38}$$

where $E_{el} = 4E_c(1 - n_g)$ and $E_{J0} = E_{J1} + E_{J2}$.

The Hamiltonian of the LC circuit is given by

$$H_v = q^2/C + (\Phi - \Phi_b)^2/2L \tag{5.39}$$

where Φ_b is the magnetic flux bias through the inductor loop caused by external magnetic field. Assuming the vibrations are slow, the total potential energy of the 'molecule' is

$$U_{\pm}(\Phi) = \pm\frac{1}{2}\sqrt{E^2_{el} + E^2_{J0}\cos^2\frac{\pi\Phi}{\Phi_0}} + \frac{(\Phi - \Phi_b)^2}{2L}. \tag{5.40}$$

Fig. 5.8 shows potential energy variation with Φ. Electronic and vibrational degrees of freedom both depend on Φ. The minimum of total potential shifts in opposite directions due to opposite slopes of qubit energies .

The basic circuitry of the measurement for the spectroscopy on the artificial molecule is shown in Fig. 5.9. The probe frequency is at $\nu_{LF} = 872$ MHz slightly below the LC oscillator frequency $\nu_0 = 874$ MHz. The reflected signal was monitored using a network analyzer which gives all the information needed for the purpose. Another drive signal ν_{HF} operating at high frequency mediates the vibronic transitions.

Below the main control parameters in this measurements are listed:

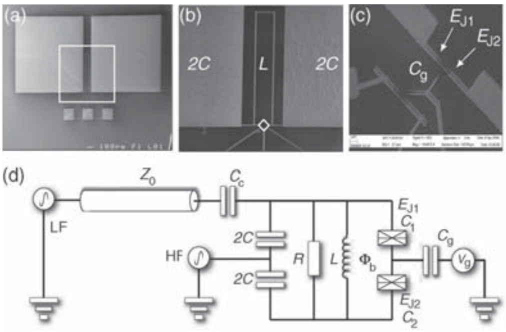

Figure 5.9. SEM image of the sample and the measurement scheme for the vibronic spectroscopy on an artificial molecule made of two JJs in combination with LC-circuitry (see Publ. V).

- Low frequency drive excites the vibration.
- High frequency drive enables vibronic transitions.

5.6 Landau Zener tunneling

Linearly driven transitions at an avoided crossing of two energy levels are known as Landau- Zener (LZ) transitions [60, 61]. An extensive review regarding LZ transition in different systems can be found in Ref. [62]. Landau-Zener tunneling which is responsible for upward transition in the BOT is also visible in other JJ based devices. According to the adiabatic theorem, a system that is initially in the ground state will remain there provided the system's parameters are changed infinitely slowly. However, when the parameters are changed at a finite rate in such a way that the two energy bands cross at least once, there is a finite probability that the system can tunnel from the lower state to the upper state. This tunneling event is known as Landau-Zener tunneling. The tunneling probability in a single sweep is given by,

$$P_{LZ} = \exp\left(-2\pi\gamma\right), \tag{5.41}$$

where $\gamma = \frac{2\pi\epsilon_{01}^2}{hv}$ and ϵ_{01} is the half of the band gap at the crossing point; v is the speed at which we pass the crossing point, $v = |d(\epsilon_0 - \epsilon_1)/dt|$, and $(\epsilon_0 - \epsilon_1) = 4E_C(1 - n_g)$ is the energy difference in the absence of the Josephson coupling.

Publ. VI gives a detailed description on the experimental studies of LZ interference on a Cooper pair box system and as well as it analyzes in the phase space the vibronic transitions performed on 'artificial molecule'.

6. Experiments on Superconducting devices

Different features of JJ based devices have been discussed in the previous chapter. In this chapter I will present the experimental results related to those devices. I will mainly concentrate on the Superconducting Cooper pair transistor (SCPT) and the Bloch Oscillating Transistor. The study on the SCPT is foremost focused into understanding its current-phase relationship which is important for realizing fast, ultra-sensitive charge and flux detectors. The main goal of the study of the BOT is to explore the region near the bifurcation point where the current gain diverges. This operation regime is very important as the tendency to bifurcate can be utilized to improve the noise performance of the BOT amplifier. In addition to developing a phenomenological understanding of the BOT near the bifurcation point, we have developed the first differential BOT pairs, which provides an essential step towards achieving a BOT-based null detector for metrological purposes.

6.1 Superconducting Cooper pair transistor

The experimental determination of Josephson inductance L_J was realized in this thesis work by the scheme depicted in Fig. 6.1; the experiment itself is described elaborately in Publ. IV.

The characteristic feature of the measurement is the insertion of the L_J into an LC circuit. By tracing the impedance of the overall circuit using microwave reflection measurements, a change in L_J can be determined because a change in inductance modifies the reflected/transmitted signal. L_m is an on-chip inductor which together with L_J forms the effective inductance L in the LC circuit: $1/L = 1/L_J + 1/L_m$. The capacitor C_c determines the coupling-strength of the driving signal to the resonator. In the scheme of Fig. 6.1,

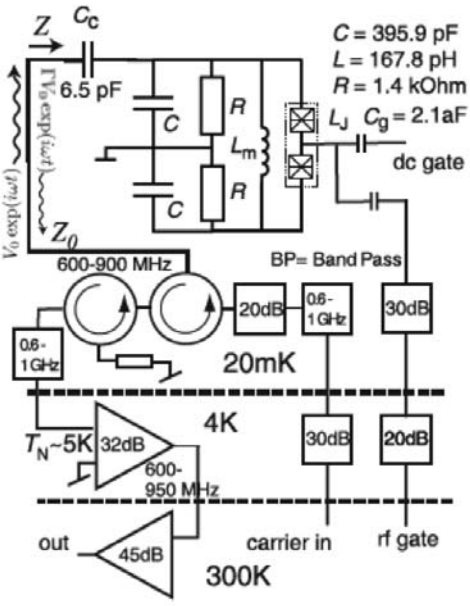

Figure 6.1. Microwave reflection measurement scheme describing the sample parameters and various setup components to determine the Josephson inductance.

Josephson inductance can be determined from the equation

$$L_J = \frac{1}{j\omega}\left\{\left[\left(\frac{1}{Z - Z_C} - \frac{1}{Z_R}\right)^{-1} - Z_R\right]^{-1} - \frac{1}{Z_L}\right\}^{-1} \tag{6.1}$$

where Z is the overall impedance seen by the input signal and $Z_{C,R,L}$ are the individual impedances of the circuit elements C, R, L; $Z_C = 1/(j\omega C_c)$, $Z_L = j\omega L$ and $Z_R = (1/R + j\omega C)^{-1}$. From experiment we measure Z to determine L_J.

In a regular tunnel junction, the current-phase relation is sinusoidal but, in other systems like point contacts and diffusive SNS junctions, this relationship does not necessarily hold. In the SCPT, we observe non-sinusoidal behavior near the charge degeneracy point. But far from the degeneracy point, the behavior is sinusoidal.

6.2 Bloch oscillating transistor

The existence of Bloch bands in JJ system lays the foundation for the realization of the Bloch oscillating transistor (BOT). This device which should not be confused with a Bloch transistor, is based on three mechanisms: Bloch oscillations, Zener tunneling and downward transition initiated by external

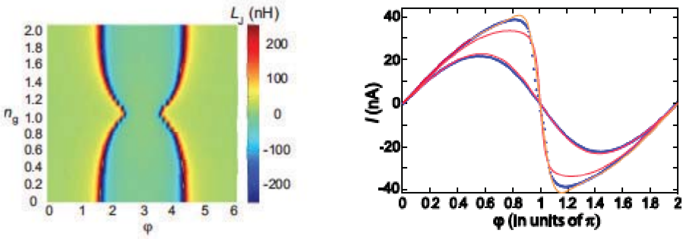

Figure 6.2. (a) L_J variation at different bias conditions (n_g, φ). (b) Non-sinusoidal behavior of current-phase relationship seen near $n_g/e = 1$ which tends to sinusoidal when moving towards $n_g = 0$. (see Publ. IV)

means, i.e., quasiparticle injection. The device can be viewed as a charge converter of single electrons, induced from the base electrode, into a sequence of N sequential Cooper pair tunneling events, i.e., Bloch oscillations on the emitter terminal with a Josephson junction. The current gain is ideally given by $\beta = 2N + 1$. The number of Bloch oscillations is limited by interband transitions caused by Landau-Zener (LZ) tunneling which depends exponentially on the band gap between the ground state and excited states of the JJ. This simple picture has been found to correspond quite well to the measured current gain. However, incoherent tunneling of Cooper pairs and electrons, complicates the basic BOT operation. The interaction of tunneling electrons or Cooper pairs with the electromagnetic environment has been demonstrated to be strong in small tunnel junctions, both in the normal and superconducting states.

Bias-induced inelastic tunneling rates can strongly modify the internal dynamics and characteristics of the BOT, e.g., leading to bifurcation in the BOT operation. A detailed introduction describing the motivation behind the study of bifurcation of BOT is given in Publ. III.

6.2.1 Experimental aspects

The key measurement to demonstrate current gain in a BOT is to measure the emitter current under voltage-biased condition across collector - emitter and to inject quasiparticles through the NIS junction. A typical $I_E - V_C$ characteristic of a BOT is shown in Fig. 6.4a. Using an external magnetic field, the E_J of the SQUID loop can be changed.

At zero base current, $I_E - V_C$ shows a Coulomb blockade which is destroyed by quasiparticle injection. We find that the blockade tends to vanish with an increase in E_J. With injection of quasiparticles, the $P(E)$ peak of $I_E - V_C$ curve becomes sharper and, eventually with large I_B, we see a sudden jump

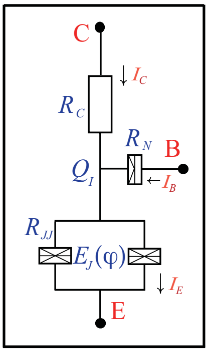

Figure 6.3. Base, emitter and collector of a BOT structure are marked by B, E and C, respectively. Positive directions for the currents are indicated by the arrows. The sample parameters are given in Table 6.1. $Q_I(t)$ is the island charge. The SQUID configuration allows tuning of the Josephson coupling energy E_J in the device.

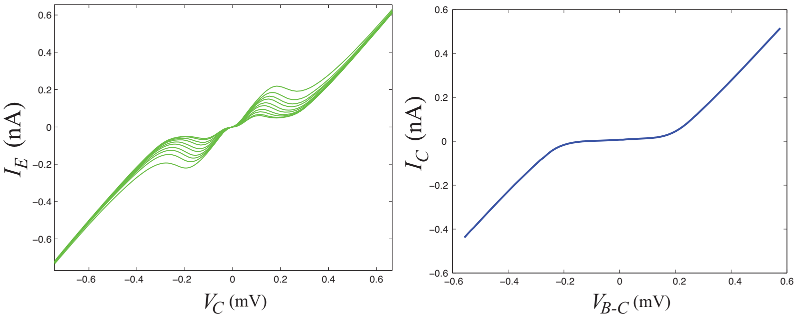

Figure 6.4. $I_E - V_C$ of BOT sample #1 at different values of E_J (see Publ. III for sample details). The right figure shows the base-collector $I - V$ characteristics of the corresponding sample.

in $I_E - V_C$ characteristics; a signature of bifurcation.

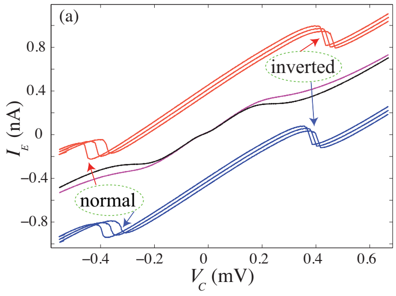

Figure 6.5. (a) Middle traces: magenta and black IV curves are measured without base current at $E_J = 6.5$ and 5.8 μeV, respectively. Red curves, corresponding to $E_J = 6.5$ μ eV, are measured at $I_B = +0.3$, +0.34, and +0.38 nA (traces from right to left). Blue curves have the same bias conditions as the red curves but were measured at $E_J = 5.8\mu$eV. The red curves are offset by (+0.22 mV,+0.42 nA) for clarity, like the blue curves by (+0.22mV,-0.42nA).

For a fixed base current $I_B \propto V_B - V_{JJ}$, V_B and V_{JJ} can each dynamically acquire two different values, while the difference can remain same. This is the reason for the bifurcation which shows up as hysteresis in the $I_E - V_C$ traces.

6.2.2 Comparison with old BOT experiments

The first report [63] on BOT presented its potential applicability as a low noise current amplifier for high source impedance systems especially when compared with solutions based on large cryogenic current comparators [64]. It was already realized that the onset of hysteresis could be utilized for improving the amplifier characteristics, but the physics behind the bifurcation were not explored. We have studied BOT dynamics in detail in the limit of $E_J/E_C \ll 1$ where the perturbation theory works well for the calculation of the Cooper pair tunneling rates. Especially, the main regime of interest was near the bifurcation. In our work we have modeled the bifurcation behavior of the BOT in current gain (β) mode with a phenomenological model and find good agreement between the model and the experimental results.

6.2.3 Fabrication and sample parameters

The basic fabrication procedure for the BOT has been already been mentioned in Ch. III and as well as explained in appendix. BOTs are fragile devices so extreme care was taken to handle these devices. The NIS junction is the most fragile part. In previous experiments, Cr was used as an intermediate layer in the NIS junction but in our current work we have not added Cr in order to avoid reduction of Δ in the superconducting island.

Table 6.1. BOT parameters for the measured samples in Publ. III. R_N and R_{JJ} are the normal state resistances of the NIS and JJ tunnel junctions in the SQUID-loop geometry, respectively. Resistances are given in units of kΩ and energies in μeV.

BOT #	R_N	R_{JJ}	R_C	E_J	E_J^{min}	E_C	Δ
1	53	27	550	17	2.7	40	150
2	75	21	305	25	3.3	60	165

6.2.4 Current gain

Injection of I_B through the base terminal changes the $I_E - V_C$ characteristics in the way shown in Fig. 6.6. Above the bifurcation point $I_E - V_C$ displays hysteretic behavior (see Fig. 6.6a). But the exact base current, I_B for this point is difficult to determine. Consequently, we plotted β^{-1} vs. I_B and

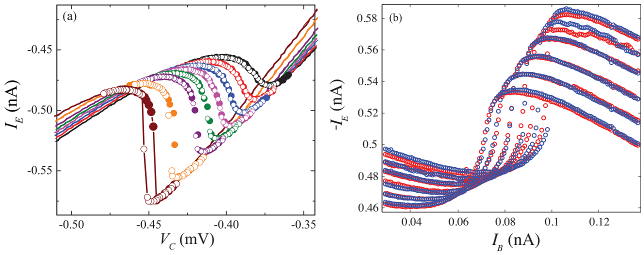

Figure 6.6. The normal operation region of the BOT at $E_J = 7.1\mu$eV with increasing I_B. Negative slope, the Landau-Zener tunneling regime, increases with I_B and eventually the slope diverges: $I_B = +0.06$, 0.065, 0.07, 0.075, 0.08, 0.085, 0.095, and 0.105 nA (from right to left). Filled (open) circle traces are for I_E when V_C is swept from left (right) to right (left). (b) Measurement of the current gain by tracing I_E vs. I_B at $E_J = 7.1\mu$eV. The steepest slope yields the operating point with the largest current gain β_E at the corresponding collector voltage V_C. V_C = - 0.443, - 0.429, - 0.419, -0.410, and -0.401 mV (traces from right to left). Different signs of I_E and I_B correspond to the regime of normal operation. Red (purple) traces are for growing (decreasing) sweep of I_B.

fitted the theoretical function (Eq. 6.2) to determine the current required for bifurcation (I_{B-H}) for different E_J:

$$\beta_E^{-1} = \frac{R_C}{V_C} \frac{\tau_\uparrow + \tau_\downarrow}{\tau_\downarrow} (-I_B + I_{B-H}) \tag{6.2}$$

A few traces of β_E^{-1} as a function of I_B are shown in Fig. 6.7.

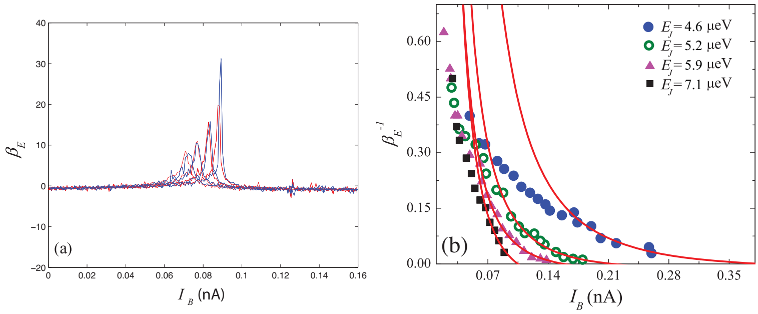

Figure 6.7. (a) Gain $\beta_E = \frac{\Delta I_E}{\Delta I_B}$ plotted against bias current I_B. (b) Inverse gain β_E^{-1} as a function of bias current I_B. Each data point was obtained from an I_E vs. I_B sweep illustrated in Fig. 6.6b. The solid curves were obtained using Eq. 6.2 fitted to the highest I_B quartile fraction of the data sets (from the first to the eighth lowest β_E^{-1} value)

6.2.5 Phase diagram for bifurcation

For two different samples (see Table 6.1), where the collector resistance R_C differed considerably, the I_{B-H} vs. E_J variation showed similar behavior. The details of the derivation of the theoretical fit are given in the appendix of Publ.

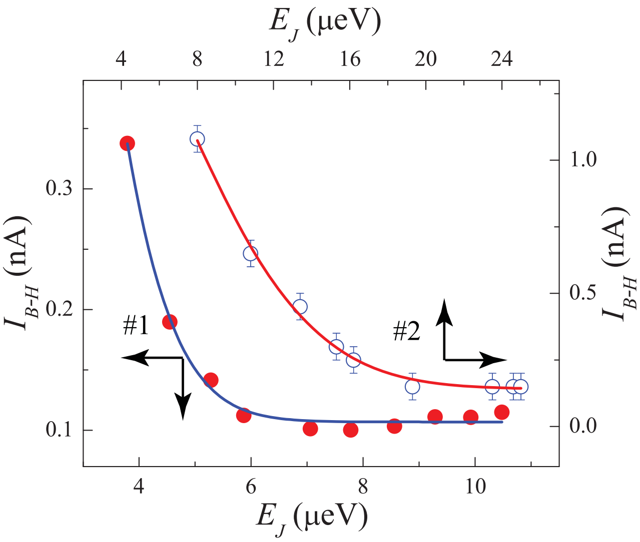

Figure 6.8. Bifurcation threshold on the E_J vs. I_B plane. Red (filled) and blue (open) circles denote the I_{B-H} values for the two BOT samples, respectively. Solid curves display the theoretical dependence from Eq. 6.3.

III. Here I write down only the final result for the phase boundary:

$$I_{BH} \propto e\frac{\Gamma_{se\uparrow} + \exp(-\kappa E_J^2)}{\sqrt{1+\Gamma_B^2/E_J^4}}. \tag{6.3}$$

In the operating regime near the bifurcation point, the base current consists of two parts; one which does not induce inter-band transitions and a smaller part which leads to transitions. The ratio of these two parts is N_e. In our model, the current gain is simply related to N_e and upward tunneling rate $\Gamma_\uparrow$.

6.2.6 Computational modeling of BOT

The simulation model of BOT is based on the Ref. [65]. It is assumed that the current flowing in the different branches can be treated separately and dynamics of island charge Q_I is simulated and averaged over a large number of steps. The tunneling rates in the JJ and NIS are calculated using $P(E)$ theory at the instantaneous charge and voltage values in the system. The tunneling at each point in time in simulation is determined by comparing a random number and the tunneling probability of the different junctions, which depends on the voltage across them. Another assumption $E_J \ll E_C$ enables the energy bands to be approximated as parabolas. In this case the quasicharge is equal to the island charge which is also the charge over the JJ. Hence, $Q_I = V_I C_{JJ}$, where V_I is the island potential. The simulated island charge can be determined by integrating over time from the equation

$$\frac{dQ_I}{dt} = \frac{V_C - V_I}{R_C} - \left(\frac{dQ_I}{dt}\right)_{QP1} - \left(\frac{dQ_I}{dt}\right)_{QP2} - \left(\frac{dQ_I}{dt}\right)_{CP}. \tag{6.4}$$

Thus, the island charge is governed by three extra factors in addition to the collector-island voltage; quasiparticle current through the base, quasiparticle current through the JJ, and Cooper pair tunneling through the JJ. This modified version of the $P(E)$ theory can be called “time dependent $P(E)$ theory”. In the simulation, the $P(E)$ is calculated considering only the real part of the impedance. The simulation run time was chosen to be longer than the time constant due to the base resistance and the capacitance from base to ground so that a steady state was reached properly. Moreover, we monitored the tunneling events on and off the island with time which revealed the ground state and the transitions to higher states. We counted all the events and the number of inter-band tunneling events to higher states in order to determine $\langle N_e \rangle$.

6.3 Common mode rejection with matched BOT pair

Common mode rejection ratio or CMRR is a measure for the capability of canceling common mode signals. A typical differential amplifier consists of two identical amplifiers with inverted gain. The work, which will be described in the following will use of two nearly identical BOTs to form a differential amplifier. Each BOT was characterized first by measuring separately $I_E - V_C$ with different I_B as described in the previous section. In Fig. 6.9 we describe the underlying idea of applying BOTs for differential amplification. For two ideal BOTs, the basic characteristics are exactly the same. The two BOTs are biased in the opposite configurations at $-I_{E_1}, -V_C, +I_B$ and $+I_{E_2}, +V_C, -I_B$, respectively. Thus, summing of the two output currents will yield $I_{E_2} - I_{E_1}$. If a base current ΔI_B is injected to the common port connected to both base electrodes then $I_E - V_C$ (Fig. 6.9b) will show upward shift as shown by the arrow. Similarly, other BOTs $I_E - V_C$ will shift downwards. Thus, summing the I_Es in two opposite directions results in net output current $I_{E_2} + \beta(\Delta I_B) - I_{E_1} - \beta(\Delta I_B) = I_{E_2} - I_{E_1}$. Thus, it rejects any common mode signal. Above principle works for ‘normal’ as well as for ‘inverted’ operation points of the BOT. The measurement schematic is shown in Fig. 6.11.

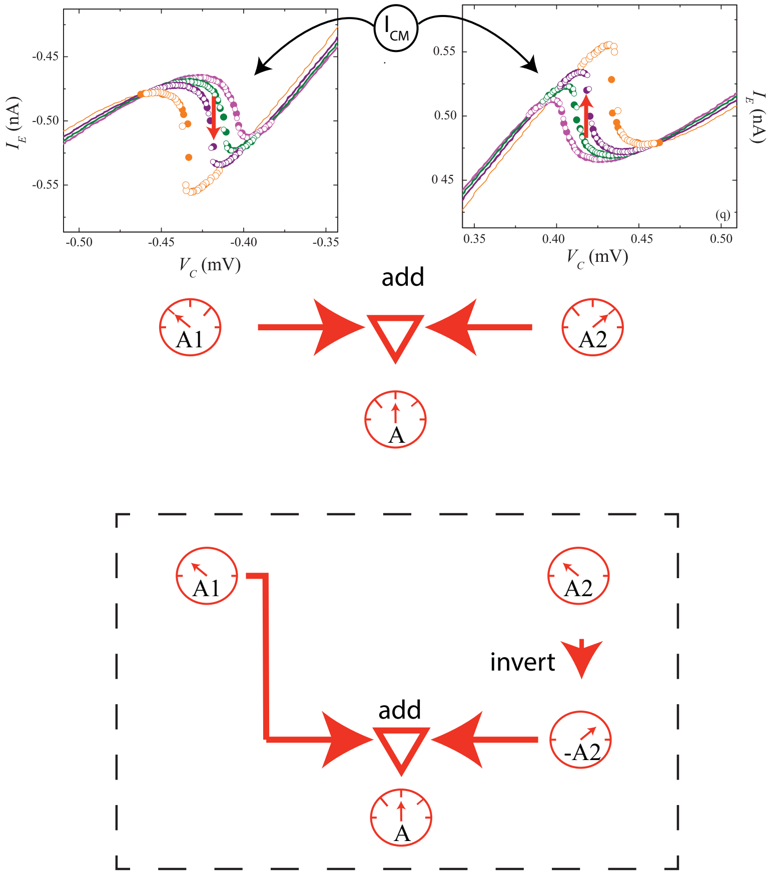

Figure 6.9. The principle for common mode rejection using a BOT pair. The right data is original data from the measurement. The data are mirrored on the left to demonstrate the capability to use a BOT pair for common mode rejection.

6.3.1 Samples

The sample fabrication is described in details in Ch. III. We followed this procedure and made samples in batches of hundreds. Even though the nominal process parameters in the fabrication steps were the same, the individual sample parameters still differed substantially as can be seen in Tab. 6.2 describing the parameters of the measured differential pair BOT. The underlying reason was attributed to nonuniform bending of the Ge mask (see Fig. 8.1) during the etching process that was employed to create the large undercut. Due to this reason, angle evaporation of different metals did not produce exactly identical sample structures among all the samples on one chip. This incapability of fabricating identical structures is the main reason that we could not achieve a fully matched differential amplifier pair for totally eliminating fully common mode current signals.

Table 6.2. Parameters for the measured differential BOT pair. R_N and R_{JJ} are the normal state resistances of the NIS and JJ tunnel junctions (SQUID), respectively. BOT #1 is the same as BOT #1 in the Table 6.1. E_J denotes the Josephson energy of the SQUID and E_C is the charging energy associated with the total capacitance (C) of the system.

BOT #	$R_N(k\Omega)$	$R_{JJ}(k\Omega)$	$R_C(k\Omega)$	$E_J(\mu eV)$	$E_C(\mu eV)$
1	53	27	550	17	40
2	123	19	660	18	45

6.3.2 Measurement

We focused our studies on the effect of output current when the base is fed with voltage. The underlying idea is similar to the idea of common mode current rejection as described in Fig. 6.9. In our experiment, we have measured I_{E1} and I_{E2} against the common mode voltage V_{CM}. Within the dashed rectangle we present the technique to be followed in real application where two currents I_{E1} and I_{E2} could be subtracted using a comparator.

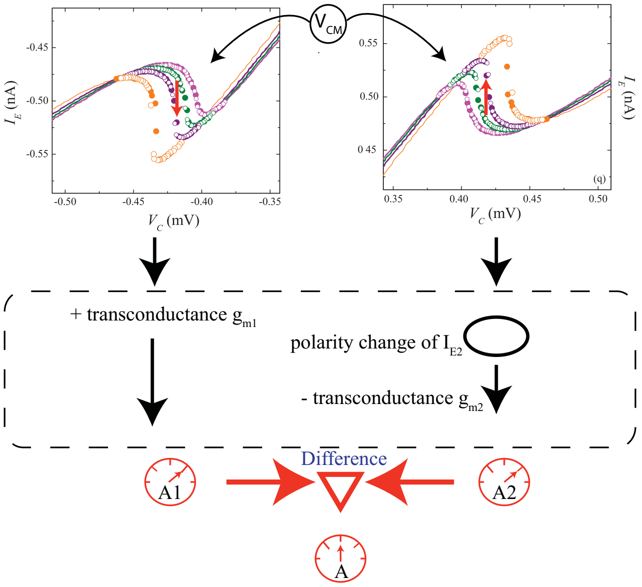

Figure 6.10. The idea which drove us to measure the common mode rejection in transconductance mode. The transconductance is of same sign for both of the BOTs. In a real experiment the polarity of one emitter current can be converted by means of a SQUID. In our experiment we are not implementing the part which is in the dashed-rectangle.

In our experiment, when the common mode (CM) port was grounded via a voltage source, most of the bias current at base passes through resistor R in Fig. 6.11 thus one needs large V_B to bias the BOTs at the operating point.

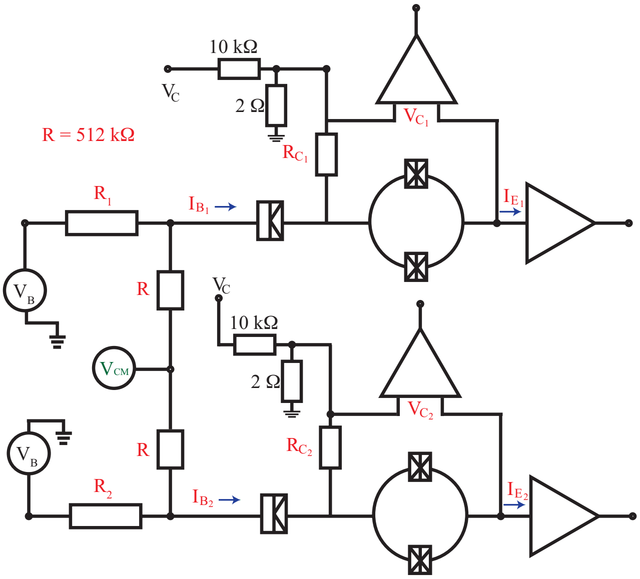

Figure 6.11. The scheme followed to determine the common mode rejection ratio of a differential BOT pair in transconductance mode.

The grounding also makes the $I - V$ characteristics smoother, which suggests the use of the ‘inverting’ operating point for these experiments as the response is sharper there as seen in Fig. 6.12. The slope is about 8 times larger for example at (-3V/5 GΩ) of the green trace in Fig. 6.12 at inverting operating point (shaded area) than the corresponding normal operating point.

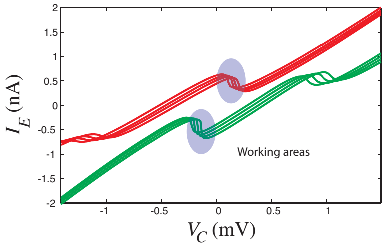

Figure 6.12. $I - V$ of the two BOTs in the common mode experiment. The shaded regions $+I_{E1}$(red trace) and $-I_{E2}$ (green trace) are the working areas. Green traces are at V_{B2} =-3,-3.5,-4,-4.5V (right to left) with $R_1 = R_2 = 5$ GΩ. Similarly, for red traces $V_{B1} = +5, +5.5, +6, +6.5$V. $V_{CM} = 0$ in the above case. We can independently tune the V_Bs to optimize the operating points.

In this configuration ($R_1 \gg R$), the base is effectively voltage biased and, instead of current gain, transconductance is employed to explain our device properties. Transconductance (g_m) is defined as $-\frac{\Delta I_E}{\Delta V_B}$. A typical g_m variation as we approach the operating point is shown in Fig. 6.13. We performed similar measurements for both of the BOTs to find the working point. We can independently tune the g_ms of the two BOTs with (V_B, V_C) combination. Moreover, in a separate measurement we measured the current through R, and calculated input impedance the $Z_{in} = \frac{\Delta V_B}{\Delta I_B}$.

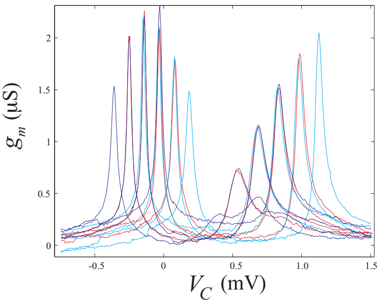

Figure 6.13. Transconductance (g_m) vs V_C traces at different V_Bs are plotted. The working point is selected in $V_B - V_C$ plane where g_m is maximum.

6.3.3 Common mode rejection ratio

For a differential BOT, we define the signal as the difference in emitter currents of the two BOTs. In a real application one can amplify the signal, e.g., by transforming the currents to magnetic fluxes with opposite polarities in a SQUID amplifier. The common mode rejection ratio is defined as $-20log\left(2\frac{|g_{m1}|-|g_{m2}|}{|g_{m1}|+|g_{m2}|}\right)$ when the magnitude of the V_B is the same. Due to the opposite bias in the non-hysteretic regime, we can have both transconductances nearly equal. If $g_{m1} = g_{m2}$, the emitter current difference $I_{E1} - I_{E2}$ would be fully independent of the common mode signal and CMRR is ∞. Fig. 6.14 shows the effect of V_{CM} on the difference current $I_{E1} - I_{E2}$. The two BOTs were biased where they have almost equal transconductance $g_{m1} = 1.9$ μS and $g_{m2} = 2.1$ μS. We find a value of CMRR = 20 dB.

6.3.4 Noise measurement

We measured the low frequency noise spectrum of the differential BOT pair with spectrum analyzer as illustrated in Fig. 6.15. The measurement was done at 'normal' operating point. As β_E increases, the noise power increases but input referred noise decreases as seen from the following equation:

$$i_n \approxeq \frac{12e}{\sqrt{R_C C}} \frac{R_{JJ}}{R_C} \beta_E^{-1} \propto \frac{1}{\beta_E}. \tag{6.5}$$

From the output noise spectra we can determine the input referred noise i_n. Fig. 6.16a shows the input noise i_n at $\beta_E = 35$ in current gain mode. The high

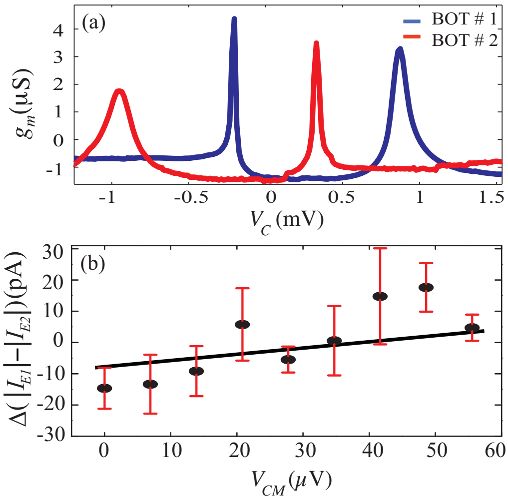

Figure 6.14. (a) Transconductance g_m of the BOTs vs. collector bias V_C. At the operating point g_m is at maximum. (b) Difference of absolute output currents of the BOTs, $\Delta(|I_{E1}| - |I_{E2}|)$ plotted versus voltage applied to the CM port. The straight line yields a CMRR of 20 dB.

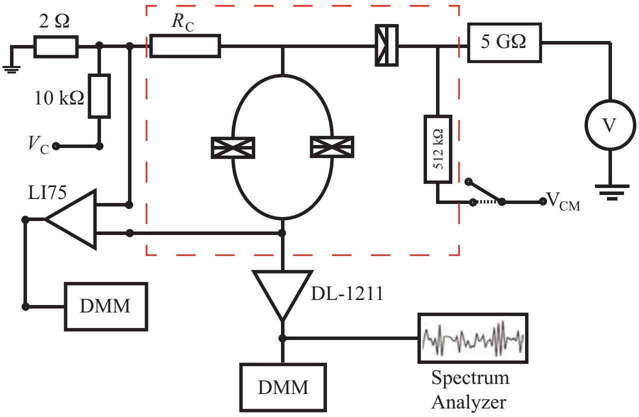

Figure 6.15. The scheme for BOT noise measurements. The dashed connection is used to measure noise in transconductance mode. The components within the dashed rectangle are located at 90 mK. DMM stands for digital multimeter.

input impedance of the device on the order of MΩ sets the low bandwidth of the device in current gain mode.

Comparison of noise in current gain mode and transconductance mode:

In the transconductance mode noise was measured at 'inverted' operating point because the performance on the normal side was poor. Noise measurement in current gain mode and transconductance mode could also be employed to determine the bandwidth of the device. We see in current gain mode that the bandwidth is reduced to 20 Hz which is consistent with the *RC* input

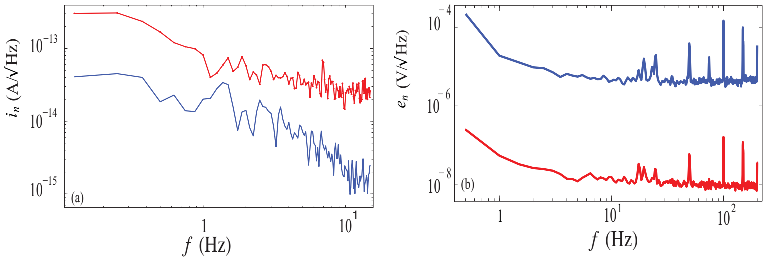

Figure 6.16. (a) Input referred current noise (i_n) in the current gain mode: red trace displays i_n with $\beta_E = 1$ i.e., far from the active operating regime. The blue curve depicts in measured at $\beta_E = 35$. (b) Input referred voltage noise (e_n) in the transconductance mode: the blue curve is obtained at $g_m = 10$ nS while the red trace was measured at $g_m = 10$ μS. Note the different frequency spans of the frames (a) and (b).

time constant of input impedance $Z_{in} \sim 10$ MΩ. We determined the input impedance $Z_{in} = 6$ MΩ which is close to the optimum impedance $Z_{opt} = \frac{e_n}{i_n}$.

In the transconductance mode the output current noise is $g_m e_n \sim 100$ fA/$\sqrt{\text{Hz}}$ which sets the criteria for the post-amplification. This transconductance amplifier works for the source resistance range 1 M $\Omega < R_s \leq Z_{opt} \sim 5 - 10$ MΩ.

7. Summary and outlook

This thesis covers a wide range of work done on Josephson junction based devices along with a comprehensive study of current-current correlations in diffusive multi-terminal conductors. The work related with Josephson junctions can be summed up in three main paths: 1) measurements of the Josephson inductance in a superconducting Cooper pair transistor in order to determine the field- and flux-dependent current-phase relationship in such a device; 2) spectroscopic microwave measurements on an artificial molecule where vibronic transitions in a JJ based qubit coupled to a LC oscillator were demonstrated for the first time and found to follow the Franck-Condon principle; 3) the dynamics of Bloch oscillating transistor was investigated near its bifurcation point, and its noise and gain characteristics were analyzed in single-ended and differential configurations.

The second theme of this thesis deals with shot noise and current-current cross correlation measurements in the frequency range of 600-900 MHz. Shot noise experiments were employed for sample characterization and for in-situ temperature determination, while current-current cross correlations were employed to look for interference phenomena in a multiterminal diffusive system. In these experiments, many of the theoretical predictions made about 15 years ago on Hanbury-Brown and Twiss type of interference effects in diffusive metals could be verified. These experiments form the first set of measurements on interference effects using "real" electrons, in contrast to the edge channel electrons propagating in 2-dim GaAs systems at high fields.

Both research themes posed various challenges on the sample fabrication in this thesis work. Various designs using 2-4 angle evaporation with extensive resist undercuts and large inclination angles were developed. The designs allowed, among other things, to fabricate devices where effective thermal reservoirs are right next to the mesoscopic sample, which is important when controlling hot-electron issues in current-current correlation experiments.

Our work on the Bloch Oscillating transistor demonstrated its capacity to work as a current amplifier suitable for cryogenic applications. Furthermore, by matching the transconductance values of two BOTs, differential pairs can be constructed that will perform well in applications where common mode issues pose problems. Altogether, I believe that differential BOT pairs form excellent null indicators for high impedence technological applications, like the closing of the metrological triangle, where current noise of 1 $\mathrm{fA}/\sqrt{\mathrm{Hz}}$ around 1 Hz frequency is the requirement for successful operation. The closing of the quantum triangle will be an important step towards the redefinition of the current standard in the SI system.

The cross-correlation work has also paved the way to experiments on multiterminal graphene systems which are underway presently at LTL. In future, I believe similar measurements will be performed even on surface states in topological insulators.

8. Appendix

8.1 Details of Bloch oscillating transistor fabrication

In the fabrication of the Bloch Oscillating Transistor, the silicon substrate is coated twice with LOR 3B resist: each spinning at 4000 rpm for 60 sec gave 400 nm of thickness. Before and after the end resist spinning the substrate was baked at 170^0C for 15 min. Next, a 30-nm Ge layer was evaporated at 0.2 Å/s rate. 3% PMMA 950K in anisole was spun on top of the Ge layer. Though normally PMMA baking is done at 180^0C for 30 min, we found that the Ge-layer tended to crack at this step. Consequently, PMMA baking was done for 5 min at 150^0C. The rate of evaporation of Ge was also found to be crucial to prevent cracking of the germanium layer. A low deposition rate of 0.2 Å/s was found to be optimal in our case. After the e-beam exposure, the chips were developed for 10sec in MIBK:IPA (1:3) which opens up a window for the Ge etching. Ge was etched in CHF_4 plasma in an RIE etcher. In the process, the PMMA was also etched away which eventually led to a bilayer resist structure with the etched Ge as the top layer and the LOR as the bottom layer. Next these chips were subjected to O_2 plasma in a temperature controlled ICP-RIE. In this etching process, temperature is a crucial parameter. In order to control the etching rate of the LOR, the sample was kept at 21^0C.

In a process involving Ge as the top layer, one cannot use optical microscope to determine the amount of undercut. An SEM micrograph of a typical Ge mask for BOT samples is shown in Fig. 8.1. We noticed that there is a high chance of bending of the mask in the etching process. Thus, one has to be careful in choosing the time and temperature for the etching process. This uncontrolled bending is the main problem in achieving identical BOT samples even with batch processing. As seen in Ch. 6 (Tabl. 6.2) the sample parameters are typically not the same though the devices were processed in the same batch.

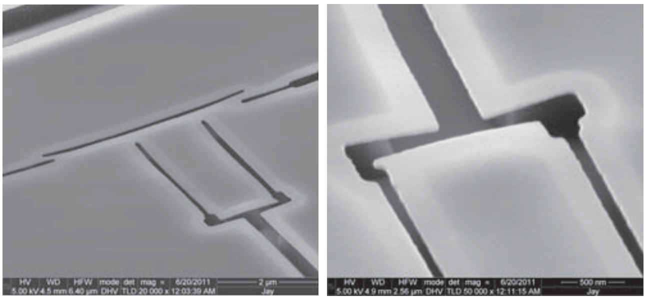

Figure 8.1. SEM micrograph of a Ge mask featuring the structure of BOT design after the final etching.

8.2 Calibration of the shot noise set-up

The noise measurements in this thesis work were performed at microwave frequencies. This gives the benefit of avoiding $1/f$ noise in the measurement. In addition to this, large bandwidth compensates for long integration times as noise-sensitivity goes inversely proportional to $\sqrt{\mathrm{BWt}}$. Thermal noise measurements on a resistor will result in white noise with spectral density $S_I = 4k_BT/R\Delta f$, which depends only on resistance R and temperature T of the resistor. The linearity of noise power with temperature has been employed in our experiments for the calibration of the noise setup. In principle, any resistor would work for this purpose but we have chosen a high quality 50 Ω resistor to match the 50 Ω impedence of the coaxial line. The resistor was pre-checked at low temperature and was found to be accurately 50 Ω over the temperature range used in our measurements. For thermal noise measurement, there was no need to bias the 50 Ω terminator as would be the case for a tunnel junction calibration.

As there was no vacuum chamber in the employed dipstick cryostat, it was cumbersome to measure noise at different temperatures. Lifting the cryostat at different heights to change the temperature would lead to another problem in this case, as the LNA and circulator would experience different temperature than the sample temperature. That would lead to uncertainty in determination of noise temperature (T_N) and bandwidth of the amplifiers and circulators. Therefore, we chose to locally heat the resistor. The schematic and along with the realization are shown in Fig. 8.2. We used a cylindrical copper block and wound a heater wire around it uniformly with GE-varnish to ensure good thermal conduction. On one side of the copper block we mounted the 50Ω resistor. The diode and the resistor were almost equally far from the center of the copper block so that the diode would determine the same temperature as would be at the resistor location. The benefit of the local heater is that it only heats up the sample while the rest of the setup will remain at 4.2 K.

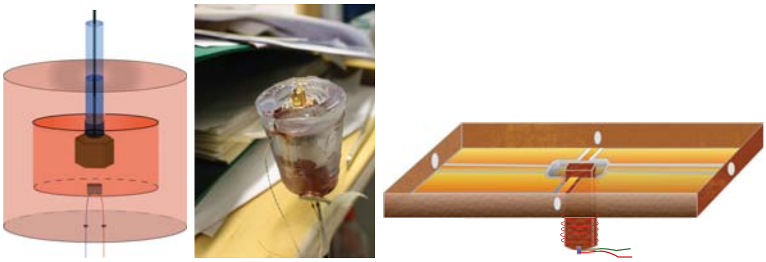

Figure 8.2. Schematic and actual set up for the thermal calibration with 50Ω. The scheme as shown in the right most figure was used to measure the sample at different temperatures using local heater.

Thermal measurement on a 50 Ω resistor was performed to calibrate the shot noise setup. $S_I - T$ data can be used to obtain the Fano factor from the shot noise data $S_I - I$ in the following way.

$$F_{DUT} = \frac{\left(\frac{\Delta S}{\Delta I}\right)_{DUT}}{2eZ_0 \left(\frac{\Delta S}{\Delta T}\right)_{Z_0} \frac{1}{4k_B}} \tag{8.1}$$

This relation works for the impedences $\sim 50\Omega$.

Similar measurement was done with a tunnel junction too. A bias-tee was inserted to simultaneously DC bias the sample and to measure the shot noise from the RF-port of the bias-tee. Most of the samples studied in our case are of low impedances, so calibration with high impedance tunnel junction needs a correction factor, called coupling factor correction, before the actual noise power could be calculated. A good quality tunnel junction is essential in this process of calibration as pinholes can reduce the measured shot noise power. In this regard, Johnson noise calibration is a more reliable way to calibrate a shot noise set up.

Bibliography

[1] S. Kogan. *Electronic noise and fluctuations in solids* . Cambridge University Press, Cambridge, 1996.

[2] Ya. M. Blanter and M. Büttiker. Shot-noise current-current correlations in multiterminal diffusive conductors. *Phys. Rev. B*, 56(4):2127, 1997.

[3] E. V. Sukhorukov and D. Loss. Noise in multiterminal diffusive conductors: Universality, nonlocality, and exchange effects. *Phys. Rev. B*, 59:13054, 1999.

[4] W. Schottky. Über spontane Stromschwankungen in verschiedenen Elektrizitätsleitern. *Ann. Phys. (Lp)*, 57:541, 1918.

[5] T. Martin. Noise in mesoscopic physics, Nanophysics: Coherence and transport. *Proceedings of Les Houches Summer School*, 2004.

[6] R. B. Laughlin. Anomalous Quantum Hall Effect: An Incompressible Quantum Fluid with Fractionally Charged Excitations . *Phys. Rev. Lett.*, 50:1395, 1982.

[7] R. de Picciotto, M. Reznikov, M. Heiblum, V. Umansky, G Bunin, and D. Mahalu. Direct observation of a fractional charge. *Nature*, 389:162, 1997.

[8] M. Reznikov, R. de Picciotto, T.G. Griffiths, M. Heiblum, and V. Umansky. Observation of quasiparticles with one-fifth of an electron's charge. *Nature*, 399:238, 1999.

[9] J. B. Johnson. Thermal agitation of electricity. *Phys. Rev.*, 32:97, 1928.

[10] H. Nyquist. Thermal agitation of electric charge in conductors. *Phys. Rev.*, 32:110, 1928.

[11] T. Martin and R Landauer. Wave-packet approach to noise in multichannel mesoscopic systems. *Phys. Rev. B*, 45:1742, 1992.

[12] R. Landauer. Spatial Variation of Currents and Fields Due to Localized Scatterers in Metallic Conduction. *IBM J. of Res. and Dev.*, 1:223, 1957.

[13] S. Datta. *Electronic Transport in Mesoscopic Physics.* Cambridge University Press, 1995.

[14] C. W. J. Beenakker and M Büttiker. Suppression of shot noise in metallic diffusive conductors. *Phys. Rev. B*, 46:1889, 1992.

[15] G. B. Lesovik. Excess quantum noise in 2D ballistic point contacts. *JETP Lett.*, 49:592, 1989.

[16] M Büttiker. Scattering theory of current and intensity noise correlations in conductors and wave guides. *Phys. Rev. B*, 46:12485, 1992.

[17] R. Hanbury-Brown and R. Q. Twiss. A New Type of Interferometer for Use in Radio Astronomy. *Philos. Mag.*, 45:663, 1954.

[18] R. Hanbury-Brown and R. Q. Twiss. Correlation between Photons in two Coherent Beams of Light. *Nature (London)*, 177:27, 1956.

[19] R. Hanbury-Brown and R. Q. Twiss. A Test of a New Type of Stellar Interferometer on Sirius. *Nature*, 178:1046, 1956.

[20] C. Von Jönsson. Elektroneninterferenzen an mehreren künstlich hergestellten feinspalten. *Zeitschrift für Physik*, 161:454, 1961.

[21] P. Rodgers. The double-slit experiment. *Physics World*, page 15, 2002.

[22] A. Tonomura, J. Endo, T. Matsuda, T. Kawasaki, and H. Ezawa. Demonstration of singleelectron buildup of an interference pattern. *American Journal of Physics*, 57:117, 1989.

[23] P. G. Merli and G. Missiroli, G. F. Pozzi. Electron interferometry with the elmiskop 101 electron microscope. *Journal of Physics E: Scientific Instruments*, 7:729, 1974.

[24] http://en.wikipedia.org/wiki/Michelson_interferometer.

[25] M. O. Scully and M. S. Zubairy. *Quantum Optics*. Cambridge University Press, 1997.

[26] T. Jeltes, J. M. McNamara, W. Hogervorst, W. Vassen, V. Krachmalnicoff, M. Schellekens, A. Perrin, H. Chang, D. Boiron, A. Aspect, and C. I. Westbrook. Comparison of the Hanbury Brown-Twiss effect for bosons and fermions. *Nature*, 445:402, 2007.

[27] Ya M. Blanter and M. Büttiker. Shot noise in mesoscopic conductors. *Physics Reports*, 336:1, 2000.

[28] D. T. McClure, L. DiCarlo, Y. Zhang, H. A. Engel, and C. M. Marcus. Tunable Noise Cross Correlations in a Double Quantum Dot. *Phys. Rev. Lett.*, 98:056801, 2007.

[29] E. V. Sukhorukov and D. Loss. Universality of Shot Noise in Multiterminal Diffusive Conductors. *Phys. Rev. Lett*, page 4959, 1998.

[30] F. Giazotto, T. Heikkilä, A. Luukanen, A. Savin, and J. Pekola. Opportunities for mesoscopics in thermometry and refrigeration: Physics and applications. *Rev. of Mod. Phys.*, 78:217, 2006.

[31] K. E. Nagaev. Influence of electron scattering on shot noise in diffusive contacts. *Phys. Rev. B*, 52:4740, 1995.

[32] D. Gutman and Y. Gefen. Shot noise in disordered junctions: Interaction corrections. *Phys. Rev. B*, 64:205317, 2001.

[33] Y. V. Nazarov and Y.M. Blanter. *Quantum Transport: Introduction to Nanoscience*. Cambridge University Press, 2009.

[34] S. A. Van Langen and M. Büttiker. Quantum-statistical current correlations in multilead chaotic cavities. *Phys. Rev. B*, 56(4):R1680, 1997.

[35] T. Heikkilä. *The Physics of Nanoelectronics*. Oxford University Press, 2013.

[36] A. H. Steinbach, J. M. Martinis, and M. H. Devoret. Observation of Hot-Electron Shot Noise in a Metallic Resistor. *Phys. Rev. Lett*, 76:3806, 1996.

[37] P. Virtanen. Phonons and shot noise. Master's thesis, Helsinki University of Technology, 2005.

[38] K. E. Nagaev. On the shot noise in dirty metal contacts. *Phys. Lett. A*, 169:103, 1992.

[39] Y. Naveh, D. V. Averin, and K. K. Likharev. Shot noise in diffusive conductors: A quantitative analysis of electron-phonon interaction effects. *Phys. Rev. B*, 58:371–374, 1998.

[40] A. Sergeev and V. Mitin. Electron-phonon interaction in disordered conductors: Static and vibrating scattering potentials. *Phys. Rev. B*, 61:6041, 2000.

[41] http://www.krytar.com/pdf/technotes/technote6.pdf.

[42] J. Bardeen, L. N. Cooper, and J. R. Scrieffer. Theory of Superconductivity. *Phys. Rev.*, 108:1175, 1957.

[43] R. P. Feynman. *The Feynman Lectures on Physics*. Addison-Wesley, 1965.

[44] B. D. Josephson. Possible new effects in superconductive tunneling. *Phys. Lett.*, 1:251, 1962.

[45] V. Ambegaokar and A. Baratoff. Tunneling between superconductors. *Phys. Rev. Lett.*, 11:104, 1963.

[46] G. Schön and A. D. Zaikin. Quantum coherent effects , Phase transitions , and the Dissipative dynamics of ultra small tunnel junctions. *Phys. Rep.*, 198:237, 1990.

[47] K. Likharev and A. B. Zorin. Theory of the Bloch-wave oscillations in small Josephson junctions. *J. Low. Temp. Phys.*, 347:59, 1985.

[48] N. W. Ashcroft and N. D. Mermin. *Solid State Physics*. Saunders College Publishers, 1976.

[49] K. K. Likharev and A. B. Zorin. Theory of the Bloch-wave oscillations in small Josephson junctions. *Journal of Low Temperature Physics*, 59:347, 1985.

[50] A. D. Zaikin and D. S. Golubev. Effect of environment on interband tunneling in ultrasmall Josephson junctions. *Physics Letters A*, 164(3-4):337–344, 1992.

[51] G. L. Ingold and Yu. V. Nazarov. *Single Charge Tunneling*. Plenum Press, New York, 1992.

[52] D. V. Averin, A. B. Zorin, and K. Likharev. Bloch oscillations in small Josephson junctions. *Sov. Phys. JETP*, 407:61, 1985.

[53] J. Clarke, A. N. Cleland, M. H. Devoret, D. Esteve, J. M. Martinis, and J. Clarke. Quantum Mechanics of a Macroscopic Variable. *Science*, 239:992, 1988.

[54] D. V. Averin and K. K. Likharev. *Mesoscopic Phenomena in Solids.* Elsevier, Amsterdam, 1991.

[55] H. Watanabe and T. Inoshita. Superatom: A novel concept in Material Science. *Optoelectronics: Devices and Technologies*, 1:33, 1986.

[56] M. A. Kastner. Artificial Atom. *Physics Today*, 46:24, 1993.

[57] J. Franck. Elementary processes of photochemical reactions. *Trans. Faraday Soc.*, 21:536, 1926.

[58] E. Condon. A theory of intensity distribution in band systems. *Phys. Rev.*, 28:1182, 1926.

[59] J. Tuorila. *Spectroscopy of artificial atoms and molecules.* PhD thesis, University of Oulu, 2010.

[60] C. Zener. Non-Adiabatic Crossing of Energy Levels. *Proceedings of the Royal Society A: Mathematical, Physical and Engineering Sciences*, 137:696–702, 1932.

[61] C. Zener. A Theory of the Electrical Breakdown of Solid Dielectrics. *Proceedings of the Royal Society A: Mathematical, Physical and Engineering Sciences*, 145:523–529, 1934.

[62] S. N. Shevchenko, S. Ashhab, and Franco Nori. Landau–Zener–Stückelberg interferometry. *Phys. Rep.*, 492:1, 2010.

[63] J Delhaye. Low-noise current amplifier based on mesoscopic Josephson junction. *Science*, 299(5609):1045, 2003.

[64] F. Gay, F. Piquemal, and G. Geneve. Ultralow noise current amplifier based on a cryogenic current comparator. *Review of Scientific Instruments*, 71(12):4592, 2000.

[65] J. Hassel and H. Seppä. Theory of the Bloch oscillating transistor. *Journal of Applied Physics*, 97:023904, 2005.

"There is plenty of room at the bottom"
-- R. P. Feynman

Aalto-DD 69/2015

ISBN 978-952-60-6207-5 (printed)
ISBN 978-952-60-6208-2 (pdf)
ISSN-L 1799-4934
ISSN 1799-4934 (printed)
ISSN 1799-4942 (pdf)

Aalto University
School of Science
Low Temperature Laboratory, Department of Applied Physics
www.aalto.fi